재료공학 박사학위논문

Computational study of hydrogen evolution reaction on defective two-dimensional transition metal dichalcogenides

이차원 전이금속 칼코겐 화합물의 음이온 공공 자리에서의 수소 발생 반응에 대한 계산 연구

2017년 8월

서울대학교 대학원

공과대학 재료공학부

이 주 희

Abstract

Computational study of hydrogen evolution reaction on defective two-dimensional transition metal dichalcogenides

Joohee Lee
Materials Sciences and Engineering
The Graduate School
Seoul National University

Hydrogen is a strong contender for a next-generation clean energy source that may replace the current fossil fuels. However, the low-cost and clean production of hydrogen source is a critical issue. In this regard, the hydrogen production by splitting water, the abundant resource on earth, may resolve many of these problems, particularly if it is driven by the solar energy. To split water using solar energy or electricity, catalysts are necessary to reduce the large overpotential during the hydrogen and oxygen evolution. For several decades, Pt is known to be the best catalyst for hydrogen evolution reaction in water splitting, but the material is very expensive and so might not be suitable for large scale applications. As such, numerous studies searched for alternative catalysts that have potential to replace Pt. Especially, transition metal dichalcogenides (TMDs) are receiving much attention as a new class of two-dimensional catalysts for hydrogen evolution reaction (HER). Despite extensive efforts to find highly efficient

catalytic TMD systems, strong candidates to replace Pt have not been suggested yet. In TMD catalysts such as MoS_2, edges are believed to be the active sites, but their limited density is a problem. Recently, it was found that the basal plane of MoS_2 can also be active for HER by introducing sulfur vacancies in addition to strain.[1] Herein, we try to identify the mechanism of HER on sulfur vacancy sites by means of kinetic Monte Carlo simulation using the energetics of first-principles calculations. We find that HER at sulfur vacancy site of MoS_2 are dominated by the Volmer-Heyrovsky mechanism, and the vacancy site can be electrically charged, thereby lowering the energy barrier of rate-limiting Heyrovsky step. In addition, when a tensile strain is applied to MoS_2, it leads to reaction paths with lower energy barriers in more negatively charged states. We also try to find new defective TMD catalyst for HER by means of computational screening based on the density functional theory. We explore the HER efficiencies of basal planes and anion vacancy sites for various TMD materials by using the hydrogen binding free energy as the descriptor for the HER efficiency. We find hydrogen binding energy is varied by the concentration of vacancy and discover good TMD candidates which are expected to show high HER performance in proper vacancy concentrations. We suggest $ZrSe_2$ and $ZrTe_2$ for low vacancy concentration, and $MoSe_2$, $MoTe_2$, WSe_2, $ReTe_2$, MoS_2 and $ReSe_2$ when intermediate or high concentration of vacancy is accessible. We expect that these materials could compete with Pt as HER catalyst even without strain engineering. In addition, through multiple linear regression, we identify that the

formation energies and the electronic structures of anion vacancies strongly affect the hydrogen adsorption energy.

Keywords: first-principles calculation, kinetic Monte Carlo, hydrogen evolution reaction (HER), transition metal dichalcogenides (TMDs), anion vacancy site, mechanism, kinetics, screening

Student Number: 2013-30184

Contents

List of tables and figures

Chapter 1. Introduction

1.1 Hydrogen as a next-generation clean energy source

Hydrogen is a strong contender for a next-generation clean energy source that may replace the current fossil fuels. There are several issues, however, ranging from the hydrogen production and storage to the efficiency of hydrogen fuel cells, which hinders a large-scale hydrogen industry.[5] In particular, the low-cost and clean production of hydrogen source is a critical issue. Currently, fossil fuels are still the main resource for the production of hydrogen due to their low costs and applicability for many fossil fuel-based machines, but the fossil fuels are limited resources and possess the problem of CO_2 and pollutants emission.[5] On the other hand, the hydrogen production by splitting water, the abundant resource on earth, may resolve many of these problems, particularly if it is driven by the solar energy. Therefore, a study on the water splitting is crucial and especially finding efficient catalysts for the oxygen evolution reaction (OER) and the hydrogen evolution reaction (HER) has great importance for the development of solar water splitting systems for the commercial production of the hydrogen fuel to replace the current fossil fuels.

1.2 2D materials as novel catalysts for water splitting

To split water using solar energy or electricity, catalysts are necessary to reduce the large overpotential during the hydrogen and oxygen evolution. For several decades, Pt is known to be the best catalyst for hydrogen evolution reaction in water splitting, but the material is very expensive and so might not be suitable for large scale applications. As such, numerous studies searched for alternative catalysts that have potential to replace Pt.[6–8] Recently, it has shown that not only the structures and compositions of the catalyst but also the dimensionality of the material is an important factor for the catalytic activity of the material. For an example, two-dimensional (2D) graphene has exceptional catalytic advantages that are absent in bulk graphite and it has been used as a novel catalyst to facilitate many chemical reactions including HER.[9–11] Also, methodologies developed by many endeavors to prepare 2D graphene has led the discovery of various other 2D materials,[12–21] which is advantageous for catalysis due to following reasons:

- High specific surface area: high density of surface active sites
- Increased hopping of electrons from the electrode to 2D catalyst surface
- Possibility to characterize the active sites on TEM or STM: good ground to combine theoretical research
- Possibility of chemical and structural modification

In addition, many conditions can affect their properties in 2D materials. There are size effect, layer thickness effect, edge and defect effect, curvature effect, and dopant and functional group effect. Especially, electronic density of states can be strongly enhanced at the edges. In addition, defects such as vacancies and dislocations can induce additional electronic states and also affect the catalytic efficiency.[17]

1.3 TMD materials for HER

Among various 2D materials, transition metal dichalcogenides (TMDs) — whose generalized formula is MX_2, where M is a transition metal and X is a chalcogen (S, Se or Te) —, most notably MoS_2, are receiving much attention as a catalyst for HER to replace platinum because of several advantages such as earth abundance and stability in the acidic media which is the HER condition.[1–4,22–54] Especially in their monolayer form, electronic structure is changed[22] and also the catalytic efficiency increases much than their bulk counterpart as the catalytic active sites might be largely exposed on the surface. Also, there is the possibility of chemical and structural modification. For example, edge or defective structure can modulate their properties. In addition, there are so many TMD compounds and their various properties ranging from metals to semiconductors that we have the possibility to choose the adequate TMDs for interested applications.

1.4 Anion vacancy as a HER active site in TMDs

The basal plane of many stable TMD phases including MoS_2 is known to be inert. This will disfavor the dissociative adsorption of hydrogen on the TMD surface, which limits HER.[55,56] Although edge sites of some TMD phases are catalytically active,[4,41,57] demands of active basal planes still exist to maximally expose the active sites. In this regard, basal planes of some meta-stable phases such as metallic T-MoS_2 are suggested as an efficient catalytic site,[3,35,55,58] but for the meta-stable phases, we cannot expect sufficient cyclic properties.

Recently, it was suggested that the basal plane of MoS_2 can also be active in the presence of sulfur vacancies.[1] It was found that the sulfur vacancies in MoS_2 could increase the catalytic activity for HER by enhancing the hydrogen adsorption, and the activity increases even further when the adequate strain was applied on the defective MoS_2. This motivated many researches that introduced vacancies, dopants, and other forms of defects in TMDs for using the material as HER catalysts.[10,29,33,37,45,47,49,59,60] In particular, Voiry et al reported largely enhanced HER property for MoS_2 basal plane by improving electronic coupling with substrate, and attribute it to activities of naturally occurring sulfur vacancies.[61]

While preceding works demonstrated catalytic activity of MoS_2 with anion vacancies, a question remains by which mechanism the anion vacancy site of TMDs gets active, how much the activity increases and how is the strain effect, or whether other TMDs may also exhibit the

enhanced HER activity when defects are introduced. Therefore, it would be timely to identify the mechanism and kinetics of HER on the anion vacancy site of TMDs, and extensively study anion vacancies in various TMDs and evaluate them as HER active sites.

1.5 Goal of the dissertation

In this dissertation, we present two different computational studies of hydrogen evolution reaction on defective two-dimensional transition metal dichalcogenides. First, we identify the mechanism of HER on vacancy site. We find out the time limiting step and investigate the overpotential dependence of the kinetics of this step. We also study the strain effect in relation to the mechanism. This study implies that engineering active sites on the inert basal planes of TMD materials would be possible by introducing anion vacancies. While the first work demonstrated catalytic activity of MoS_2 with anion vacancies, a question remains whether other TMDs may also exhibit the enhanced HER activity when defects are introduced. Therefore, it would be meaningful to extensively study anion vacancies in various TMDs and evaluate them as HER active sites. So for the second topic, we explore the HER efficiencies of basal planes and anion vacancy sites of various TMD materials by calculating hydrogen binding energy. To screen proper materials, we searched all stable TMD structures. For the screening targets, we investigate how inert basal plane of TMDs turn to be active with the anion vacancies and suggest four different types of candidate materials that are predicted to have good HER efficiencies depending on the range of the vacancy concentration. In addition, we examine the correlation of some relevant physical quantities with hydrogen adsorption energy, the descriptor for HER activity, at the anion vacancy sites.

Chapter 2. Theoretical backgrounds and methods

2.1 Density functional theory (DFT)

2.1.1 Hohenberg and Kohn theorem

Most of the electronic structure calculations of materials have been based on the density functional theory (DFT) since Hohenberg and Kohn theorem[62] was introduced in 1964. Hohenberg and Kohn theorem implies that the ground state charge density $\rho(r)$ is the necessary and sufficient information to calculate the electronic structure of materials and corresponding total energies. If the ground state density is known, Hamiltonian H, ground state wave function ψ, and ground state energy can be defined as a unique functional of $\rho(r)$.

The total energy E of the system is defined as

$$E = \int v(r)\rho(r)dr + F(\rho(r)), \tag{2.1}$$

where $v(r)$ is the external potential, $\rho(r)$ is the charge density, and $F(\rho(r))$ is the universal functional. By the variational principle, we can prove that the total energy given by Eq.(2.1) is minimum when $\rho(r)$ corresponds to the true charge density in the ground state.

To calculate the electronic structures and total energies of the material, the Hamiltonian must be defined. The Hamiltonian of electrons interacting in the ionic potential is shown in Eq.(2.2)

$$-\sum_{i=1}^{N}\frac{\hbar^2}{2m}\nabla_i^2-\sum_{i,I=1}^{N}\frac{Z_I e^2}{\left|\overrightarrow{R_I}-\vec{r_i}\right|}+\sum_{i>j}^{N}\frac{e^2}{\left|\vec{r_i}-\vec{r_j}\right|}\nabla_i^2, \tag{2.2}$$

where the first term is kinetic energy, the second term is ion-electron interaction, and the third term is electron-electron interaction. This Hamiltonian is accurate but it gives practically unsolvable Schrodinger equation because of the extremely high degree of freedom.

2.1.2 Kohn-Sham equation

In 1965, Kohn and Sham suggested the effective potential V_{eff} to convert the many-body problem to simple one particle problem. The effective potential is composed of three parts as follow:

1) Ewald energy V_{ion-e}: the ion-electron interaction

2) Hartree energy V_{e-e}: the electron-electron Coulomb interaction

3) Exchange-correlation energy V_{xc}.

$$V_{eff}(r)=V_{ion-e}+V_{e-e}+V_{xc} \tag{2.3}$$

Using the V_{eff}, the Schrodinger equation with complicated many-body interactions becomes simple one particle problem as the following equation:

$$\left[-\frac{\hbar^2}{2m}\nabla^2+V_{eff}(\rho(\vec{r}))\right]\phi_i(\vec{r})=\varepsilon_i\phi_i(\vec{r}) \tag{2.4}$$

Starting with a trial charge density and wave vectors from the atomic potentials of given system, the effective potential as a functional of the density is calculated and then Schrodinger equation is reduced to single particle equation. This equation is called Kohn-Sham equation. By

solving this equation, the Fermi energy and new charge density can be determined. This calculation process is repeated recursively until the difference between starting charge density and new charge density becomes smaller than given criteria.

2.1.3 Exchange-correlation energy

In the calculation of Kohn-Sham equation, determination of the effective potential is compulsory and very important. The exchange-correlation part of the effective potential V_{xc} is related to quantum mechanical interactions of the many-body system, and there are two different conventional approximations.

One is local density approximation (LDA) which is first introduced by Kohn and Sham.[63] The LDA assumes that the exchange-correlation energy of the system as a functional of charge density function that it is identical to the corresponding value of the homogeneous electron gas which has same local density ρ everywhere.

$$E_{xc}^{LDA}[\rho(r)] = \int \varepsilon_{xc}^{LDA}(\rho(r))\rho(r)dr \qquad (2.5)$$

where $\varepsilon_{xc}^{LDA}(\rho(r))$ is the exchange-correlation energy density of the homogeneous system as mentioned above. The LDA might be adequate for systems that have smooth electron density such as the free electron like metal or the semiconductor. However, using it to the systems that have rapidly changing electron density such as the transition metal systems which have the localized electrons could

possibly include error. Usually, the bond strength or the lattice parameter is underestimated than experiments.

The LDA could imply large errors for the system where the electron density changes rapidly because LDA sees only local electron density to evaluate the exchange-correlation energy term. Therefore, generalized gradient approximation (GGA) which considers also the gradient of electron density of the local point is introduced later on by Perdew[64] and Becke[65]. GGA is basically similar to LDA except that GGA contains the inhomogeneity of electron density considering the XC energy deviation from the uniform electron gas consumption.

$$E_{xc}^{GGA}[\rho(r)] = \int \varepsilon_{xc}^{GGA}(\rho(r)|\nabla\rho(r)|)\rho(r)dr \qquad (2.6)$$

In 1996, Perdew-Burke-Ernzerhof improved formal GGA scheme (PW91) and it is called PBE.[66] We use PBE for GGA functional in this dissertation. GGA improved the description of the physical properties like bond strength and the cohesive energy of solids compared to LDA.[67]

2.2 Gibbs free energy.

2.2.1 Gibbs free energy of intermediates of HER on V_S in MoS_2

To investigate the HER mechanism on the sulfur vacancy (V_S) of MoS_2, we refer to Kim (2016)[2] about the Gibbs free energy of intermediates which is defined as follows:

$$\Delta G([n\text{H-}V_S]^q) = E_{tot}([n\text{H-}V_S]^q] - E_{tot}([V_S]^0) + E_{sol} + \Delta\text{ZPE} + n\mu_{H^+} - (n-q)\mu_e \quad , \quad (2.7)$$

where $[n\text{H-}V_S]^q$ indicates that nH atoms are adsorbed on the sulfur vacancy with the charge state of q. In Eq.(2.7), E_{tot} and E_{sol} are the total energy and the solvation energy, respectively, and ΔZPE is the difference in zero-point energy of the adsorbed H atoms between reactants and products (0.02~0.04 eV). The spurious electrostatic interactions between periodic image charges are neglected owing to high dielectric constant of water. μ_{H^+} and μ_e in Eq.(2.7) are chemical potentials of hydrogen ion and electron, respectively, and they are defined from reference of standard hydrogen electrode. Therefore, sum of μ_{H^+} and μ_e is equal to $\frac{1}{2}\mu_{H_2}$ that is calculated as follows:

$$\mu_{H_2} = E_{tot}(H_2) + \text{ZPE}(H_2) + \Delta H - T\Delta S \quad , \quad (2.8)$$

where ΔH and ΔS correspond to the enthalpy and entropy changes per H_2 molecule between T and 0 K at standard pressure, respectively, and are obtained from thermodynamic tables. In the present work, T is set to the room temperature (298.25 K).

Chapter 3. Mechanism of HER on V_S in MoS_2

3.1 Introduction: mechanisms of HER

3.1.1 HER on V_S in MoS_2

MoS_2 has several advantages as a HER catalyst such as earth-abundance, stability in acidic media which is the HER condition, and high specific surface area that can give high density of active sites as a 2D material. However, the basal plane of MoS_2 in the stable phase (H-MoS_2) is known to be catalytically inert. In the seminal paper, Hinnemann *et al*[44] proposed that Mo-edge facets of H-MoS_2 would be active for HER because of small hydrogen binding energy (~0.1 eV) that is the value estimated as a descriptor for HER activity following the Sabatier's principle.[44] This theoretical result was confirmed by electrochemical experiments with STM observation.[57] Several experiments afterward also confirm the role of edges,[58] but when the edge sites are the only active sites, the density of active site is fairly limited. On the other hand, it was also found that metastable T-MoS_2 phase shows high catalytic activity during HER. However, we cannot expect long-term stability with the meta-stable phases.

Recently, Li *et al* reported that the basal plane of H-MoS_2 can be activated by introducing the sulfur vacancy (V_S) and applying strain.[1] By calculating the hydrogen binding energy, they identified the optimal condition of the applied strain depending on the respective vacancy

densities, which is partially confirmed by the accompanied electrochemical experiment. The applied bias to extract 10 mA/cm^2 of exchange current which is defined as overpotential was 170 mV which is larger than that of Pt, 59 mV, but smaller than 320 mV of edge sites of MoS_2 and 187 mV for meta-stable phase of MoS_2.[1,58] This indicates that the defect-induced MoS_2 basal plane is a promising catalytic system that may replace Pt.

The catalytic reaction mechanism at the semiconducting atomic-sized active sites such as V_S would be different from that at the pure metallic or semiconducting surfaces like Pt and basal planes of TMDs due to the localized defect states.[68] For the rational design of catalysts by inducing atomic-sized defects in material surfaces, it would be necessary to understand the catalytic reaction kinetics in atomistic detail. In this study, we perform multiscale simulation combining *ab initio* calculation data and kinetic Monte Carlo (KMC) simulation to investigate the HER mechanism on the sulfur defect of H-MoS_2 basal plane. We refer to Kim (2016)[2] for the Gibbs free energies along various reaction pathways from H^+ to H_2 by DFT calculations and the favorable reaction path is determined by KMC simulation considering reaction rates of all possible reaction steps. We find that H_2 evolves with Volmer-Heyrovsky mechanism at V_S site in MoS_2 and the rate-determining step is the Heyrovsky step. The Heyrovsky barrier is lower when the defect site is more negatively charged. So, when the tensile strain is applied, reaction path with lower energy barrier is more easily accessible with the more negatively charged state. The computed

turnover frequency and overpotential are in good agreement with the experimental value, and also the strain effect is well estimated.

3.2 Theoretical approaches for HER on V_S

3.2.1 Multiscale simulation

In material sciences, multiscale simulation is used to calculate material properties that we can model on a certain level of size and time scale by using data from different levels. To study the mechanism of HER on V_S in MoS_2, we have to model on the level of hydrogen evolving time scale, and also the atomic level calculation is needed to identify the dominating mechanism, For the time-evolving kinetics study, we use kinetic Monte Carlo (KMC) simulation by using atomic scale energetics based on first-principles calculation. We assume the vacancy is isolated and the interaction between sites are not considered so that we only have to trace one site by KMC.

3.2.2 HER; a stepwise chemical reaction

HER is a stepwise chemical reaction that consists of three elementary steps. Volmer, Heyrovsky, and Tafel.[37,69–72] Those steps can be expressed as

(i) $H^+ + e^- + * \rightarrow H*$ (Volmer)

(ii) $H^+ + e^- + H* \rightarrow H_2$ (Heyrovsky)

(iii) $2H* \rightarrow H_{2(g)}$ (Tafel)

In the above equation, * indicates the active site, H* and 2H* indicate one and two hydrogens adsorbed active sites, respectively. They take more than one elementary step to complete HER. An intermediate state

is the reaction product of each of these steps, except for the last one, which is called the final state. The activated complex at the saddle point of a potential energy surface is called the transition state. (See Figure 3.1)

The Volmer step can occur twice continuously on V_S site of MoS_2, as the possible number of hydrogen adsorption depends on the electronic structure of the active site. Therefore, [V_S], [H-V_S] and [2H-V_S] states are possible, where [V_S] is the hydrogen-free sulfur vacancy, [H-V_S] is the one hydrogen adsorbed sulfur vacancy, and [2H-V_S] is the two hydrogens adsorbed sulfur vacancy site. We refer the sequential adsorption steps as the first and second Volmer step, respectively.

The Heyrovsky steps are also distinguished as first and second Heyrovsky steps. In Volmer and Heyrovsky steps on MoS_2, we consider electron charging and protonation events separately due to the semiconducting material property where various discrete charge states are accessible. So, Volmer and Heyrovsky steps refer the protonation step that delivers H^+ involving an arbitrary number of electrons.

For each possible chemical state, [V_S], [H-V_S] and [2H-V_S], we can list up the possible next steps. On [V_S], hydrogen can be adsorbed by first Volmer step. When the state is [H-V_S], desorption of hydrogen is possible, and also the second Volmer step or HER by first Heyrovsky step is possible. When the state is [2H-V_S], the second hydrogen can be desorbed, and HER by second Heyrovsky step or Tafel step is also possible.

A great diversity of sequences of these steps has to be considered to estimate overall turnover frequency (TOF) of HER. Instead, we conduct KMC simulation to find TOF that comes from the spontaneously selected sequences of the elementary steps for HER.

3.2.3 Transition state theory

Transition state theory (TST) explains the reaction rates of elementary chemical reactions. The theory assumes a special type of chemical equilibrium (quasi-equilibrium) between reactants and activated transition state complexes. TST is used primarily to understand qualitatively how chemical reactions take place. The basic ideas behind TST are as follows:[73]

A. Rates of reaction can be studied by examining activated complexes near the saddle point of a potential energy surface. The details of how these complexes are formed are not important. The saddle point itself is called the transition state.
B. The activated complexes are in a special equilibrium (quasi-equilibrium) with the reactant molecules.
C. The activated complexes can convert into products, and kinetic theory can be used to calculate the rate of this conversion.

The reaction rate is expressed in TST like follows by combining Arrhenius equation and Rice's idea about pre-exponential factor[74–76]:

$$r = \frac{k_B T}{h} \exp\left(\frac{-\Delta G^{\ddagger}}{k_B T}\right) \tag{3.1}$$

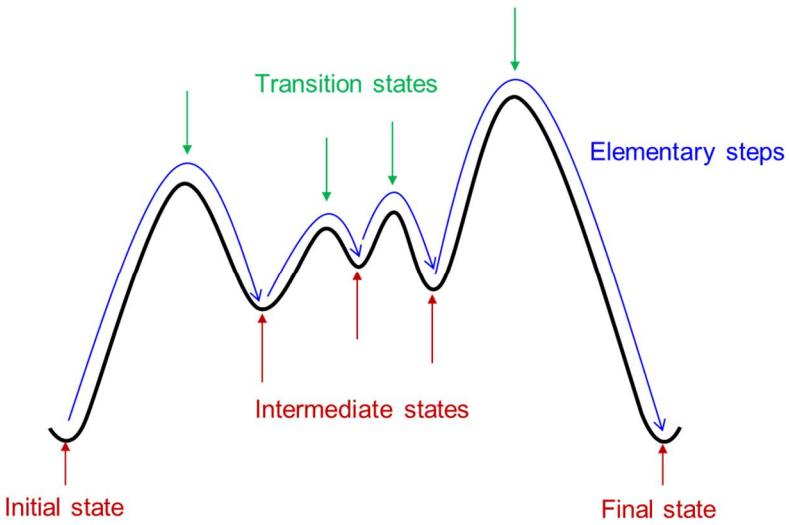

Figure 3.1 Terminology for stepwise chemical reaction like HER

3.2.4 Possible intermediate states of sulfur vacancy in the MoS_2 during HER

HER dynamics on the sulfur vacancy of MoS_2 is characterized by occasional transitions from one state to another. We also assume the vacancy is isolated that the interaction between sites is not considered. So, for the isolated vacancy, we investigate the possible chemical state during HER. On sulfur vacancy site, one or two hydrogen atom can be adsorbed by first and second Volmer steps. When the sulfur vacancy site is not terminated by hydrogen ($[V_S]^q$), the defect states are comprised of an occupied singlet a_1 and unoccupied doubly degenerate e states in neutral. So the charge state q of this state can be from -4 to +2. When one hydrogen is adsorbed ($[\text{H-}V_S]^q$), a_1 level is lowered under the valence band forming bonding state with hydrogen and an excess electron is occupied in e states and Jahn-Teller distortion occurs that e states split into e' and e'' states, so the charge state q can be from -3 to +1. When the second hydrogen is adsorbed on this site ($[\text{2H-}V_S]^q$), e' state is fully occupied and lowered below the valence band as bonding state, and charge state can be from -2 to 0.

We express the chemical state as $[n\text{H-}V_S]^q$ and 15 states are possible.

$$\begin{cases} n=0 \;\rightarrow\; -4 \le q \le +2 \\ n=1 \;\rightarrow\; -3 \le q \le +1 \\ n=2 \;\rightarrow\; -2 \le q \le 0 \end{cases} \tag{3.2}$$

Note that defect charge state can be changed when Fermi level is changed by external factors.

3.2.5 Definition of relative energies of intermediate states

To represent energetics of all possible reaction pathway, we first define relative energies of intermediate states with respect to the $[V_S]^0$. To compare the energies, we define the reaction energies from the system of $[V_S]^0$ to the system of $[n\text{H-}V_S]^q$ as $\Delta G(n,q)$, where the number of elements and electrons of initial and final states are kept same.

$$
\begin{aligned}
[V_S]^0 &\xrightarrow{\Delta G(0,2)} [V_S]^{2+} + 2e^- \\
[V_S]^0 &\xrightarrow{\Delta G(0,1)} [V_S]^{1+} + e^- \\
[V_S]^0 &\xrightarrow{\Delta \boldsymbol{G(0,0)}} [V_S]^0 \\
[V_S]^0 + e^- &\xrightarrow{\Delta G(0,-1)} [V_S]^{1-} \\
[V_S]^0 + 2e^- &\xrightarrow{\Delta G(0,-2)} [V_S]^{2-} \\
[V_S]^0 + 3e^- &\xrightarrow{\Delta G(0,-3)} [V_S]^{3-} \\
[V_S]^0 + 4e^- &\xrightarrow{\Delta G(0,-4)} [V_S]^{4-}
\end{aligned}
$$

$$
\begin{aligned}
[V_S]^0 + \mathrm{H}^+ &\xrightarrow{\Delta G(1,1)} [\text{H-}V_S]^{1+} \\
[V_S]^0 + \mathrm{H}^+ + e^- &\xrightarrow{\Delta G(1,0)} [\text{H-}V_S]^0 \\
[V_S]^0 + \mathrm{H}^+ + 2e^- &\xrightarrow{\Delta G(1,-1)} [\text{H-}V_S]^{1-} \\
[V_S]^0 + \mathrm{H}^+ + 3e^- &\xrightarrow{\Delta G(1,-2)} [\text{H-}V_S]^{2-} \\
[V_S]^0 + \mathrm{H}^+ + 4e^- &\xrightarrow{\Delta G(1,-3)} [\text{H-}V_S]^{3-}
\end{aligned}
\qquad (3.3)
$$

$$
\begin{aligned}
[V_S]^0 + 2\mathrm{H}^+ + 2e^- &\xrightarrow{\Delta G(2,0)} [2\text{H-}V_S]^0 \\
[V_S]^0 + 2\mathrm{H}^+ + 3e^- &\xrightarrow{\Delta G(2,-1)} [2\text{H-}V_S]^{1-} \\
[V_S]^0 + 2\mathrm{H}^+ + 4e^- &\xrightarrow{\Delta G(2,-2)} [2\text{H-}V_S]^{2-}
\end{aligned}
$$

where $\Delta G(0,0) = 0$, and the general form of the relative energy is as follow:

$$\Delta G(n,q) = G([n\text{H-}V_S]^q) - G([V_S]^0) - n\mu_{H^+} - (n-q)\mu_e \quad (3.4)$$

In standard hydrogen electrode (SHE) condition, a redox reaction occurs maintaining the concentration of both the reduced form and oxidized form to unity. The redox half-cell reaction is as below:

$$2H^+(aq) + 2e^- \rightarrow H_2(g)$$

$$\mu_{H^+}^{SHE} = \frac{1}{2}\mu^\circ{}_{H^2} - \mu_e^{SHE}$$
$$\mu_e^{SHE} = -4.44 \text{ eV} \quad , \quad (3.5)$$

where $\mu_{H^+}^{SHE}$ is the chemical potential of proton at SHE condition, and μ_e^{SHE} is the chemical potential of electron at SHE condition[77–79].

So, relative energy of each state is expressed as follows in SHE condition:

$$\Delta G^{SHE}(n,q) = G([n\text{H-}V_S]^q) - G([V_S]^0) - \frac{n}{2}\mu^\circ{}_{H^2} + q\mu_e^{SHE} \quad (3.6)$$

In general condition, the chemical potentials of electron and proton depend on pH and external bias η.

$$\mu_{H^+} = \mu_{H^+}^{SHE} - 0.0591pH$$
$$\mu_e = \mu_e^{SHE} + e\eta \quad (3.7)$$

So, the general form of relative energy $\Delta G(n,q)$ is represented as follows:

$$\Delta G(n,q) = \Delta G^{SHE}(n,q) + 0.0591n\boldsymbol{pH} + (q-n)e\boldsymbol{\eta} \quad (3.8)$$

We can determine all ΔG^{SHE} by DFT calculation. We refer to Kim (2016)[2] on these data. They considered solvation effect, zero-point energy (ZPE) and entropy contribution.

3.2.6 Reaction energy and kinetic barrier

Reaction energy of each elementary step of HER is defined as

$$\Delta\Delta G^{\mathrm{SHE}}(\text{intermediate step})$$

,

and we deal with electron charging separately, so the kinetic barrier is defined as follows by considering transition state of the step where the number of electrons in the system is kept same.

$$\Delta\Delta^{\ddagger}G^{\mathrm{SHE}}(\text{intermediate step}) = \Delta G^{\mathrm{SHE}}(\text{transition state}) - \Delta G^{\mathrm{SHE}}(\text{initial})$$

The kinetic barrier has no electrical bias dependence since the initial and transition states maintain the same number of electrons.

$$\Delta\Delta^{\ddagger}G^{\eta} = \Delta\Delta^{\ddagger}G^{\mathrm{SHE}} = \Delta G^{\mathrm{SHE}}(\text{transition state}) - \Delta G^{\mathrm{SHE}}(\text{initial})$$

$$= G^{\mathrm{SHE}}\big(\text{transition state}\big) - G^{\mathrm{SHE}}(\text{initial})$$

We can calculate all $\Delta\Delta^{\ddagger}G^{\mathrm{SHE}}$ by NEB or string method with constraint DFT with solvation effect.[2]

All data we used in this study for reaction energetics are obtained by Kim[2], and the data are shown in Table 3.1.

Table 3.1 All calculation data. Kim (2016)[2]

$$2H^+ + 2e^- \xrightarrow{\Delta G_{HER}} H_2$$

$$\Delta G_{HER} = -2e\eta + 0.1182pH \quad \text{at } pH = 0$$

Step	Reaction formula $[nH{-}V_S]^q + mH^+ \rightarrow [n'H{-}V_S]^{q'} + rH_2$	$\Delta G^\eta(n,q)$ (eV)	$\Delta G^\eta(n',q') + r\Delta G^\eta_{HER}$ (eV)	$\Delta\Delta G^\ddagger$ (eV)
Volmer	$[V_S]^0 + H^+ \rightarrow [H{-}V_S]^+$	0.000	0.367	0.513
	$[V_S]^- + H^+ \rightarrow [H{-}V_S]^0$	$-0.049 - e\eta$	$-0.144 - e\eta$	0.400
	$[V_S]^{2-} + H^+ \rightarrow [H{-}V_S]^-$	$0.237 - 2e\eta$	$-0.329 - 2e\eta$	0.243
	$[V_S]^{3-} + H^+ \rightarrow [H{-}V_S]^{2-}$	$0.859 - 3e\eta$	$0.052 - 3e\eta$	0.000
	$[V_S]^{4-} + H^+ \rightarrow [H{-}V_S]^{3-}$	$1.639 - 4e\eta$	$0.668 - 4e\eta$	0.000
2nd Volmer	$[H{-}V_S]^- + H^+ \rightarrow [2H{-}V_S]^0$	$-0.329 - 2e\eta$	$0.005 - 2e\eta$	1.018
	$[H{-}V_S]^{2-} + H^+ \rightarrow [2H{-}V_S]^-$	$0.052 - 3e\eta$	$-0.053 - 3e\eta$	0.660
	$[H{-}V_S]^{3-} + H^+ \rightarrow [2H{-}V_S]^{2-}$	$0.668 - 4e\eta$	$0.335 - 4e\eta$	0.395
Heyrovsky	$[H{-}V_S]^+ + H^+ \rightarrow [V_S]^{2+} + H_2$	0.367	2.575	1.309
	$[H{-}V_S]^0 + H^+ \rightarrow [V_S]^+ + H_2$	$-0.144 - e\eta$	$1.219 - e\eta$	1.098
	$[H{-}V_S]^- + H^+ \rightarrow [V_S]^0 + H_2$	$-0.329 - 2e\eta$	$0.000 - 2e\eta$	0.906
	$[H{-}V_S]^{2-} + H^+ \rightarrow [V_S]^- + H_2$	$0.052 - 3e\eta$	$-0.049 - 3e\eta$	0.669
	$[H{-}V_S]^{3-} + H^+ \rightarrow [V_S]^{2-} + H_2$	$0.668 - 4e\eta$	$0.237 - 4e\eta$	0.427
2nd Heyrovsky	$[2H{-}V_S]^0 + H^+ \rightarrow [H{-}V_S]^+ + H_2$	$0.005 - 2e\eta$	$0.367 - 2e\eta$	0.906
	$[2H{-}V_S]^- + H^+ \rightarrow [H{-}V_S]^0 + H_2$	$-0.053 - 3e\eta$	$-0.144 - 3e\eta$	0.774
	$[2H{-}V_S]^{2-} + H^+ \rightarrow [H{-}V_S]^- + H_2$	$0.335 - 4e\eta$	$-0.329 - 4e\eta$	0.644
Tafel	$[2H{-}V_S]^0 \rightarrow [V_S]^0 + H_2$	$0.005 - 2e\eta$	$0.000 - 2e\eta$	1.306
	$[2H{-}V_S]^- \rightarrow [V_S]^- + H_2$	$-0.053 - 3e\eta$	$-0.049 - 3e\eta$	1.294
	$[2H{-}V_S]^{2-} \rightarrow [V_S]^{2-} + H_2$	$0.335 - 4e\eta$	$0.237 - 4e\eta$	1.281

3.2.7 State transition diagrams of intermediate and transition states

Energies of intermediate states depend on the external bias as shown as in Table 3.1. These data can be plotted as state transition diagrams. Electron transfer is much faster than the chemical reaction steps, so we assume that the initial state of any elementary step is always in the most stable charge state. State transition diagram for Volmer step is shown in Figure 3.2a. When a negative bias is applied to the cathode of water splitting cell, the defects in cathode catalyst are charged more negatively. The minimum energy of all charge state is shown in this figure, and the energy change from the minimum of $\Delta G(n=0)$ to the minimum of $\Delta G(n=1)$ is the adsorption energy. The adsorption energy decreases with increasing bias. The energy change from the minimum of $\Delta G(n=0)$ to the minimum energy of transition states of Volmer step $\Delta^{\ddagger}G$(Volmer) is the energy barrier of the Volmer step. (See Figure 3.2b) The barrier of the Volmer step depend on the bias, it could be seen that the charge transfer coefficient, α which is defined usually in metallic catalysts corresponds to the positive value ($\alpha > 0$).

State transition diagram for Heyrovsky step is shown in Figure 3.3a. When a negative bias is applied, the charge states of the defects in catalyst change more negatively. The minimum energy of all charge state is shown in this figure, and the energy change from the minimum of $\Delta G(n=1,r=0)$ to the minimum energy of transition states of Heyrovsky step $\Delta^{\ddagger}G$(Heyrovsky) is the energy barrier of the Heyrovsky step. (See Figure 3.3b) The barrier of the Heyrovsky step depend on the external bias, so the charge transfer coefficient corresponds to the

positive value, $\alpha > 0$. The Heyrovsky barrier is always higher than Volmer barrier, so the Heyrovsky step is the rate-limiting step. So, the turnover frequency can be approximated as

$$P\left(\left[\text{H-}V_{\text{S}}\right]\right) \cdot \sum_{i}^{\text{Heyrovsky}} r_i \tag{3.9}$$

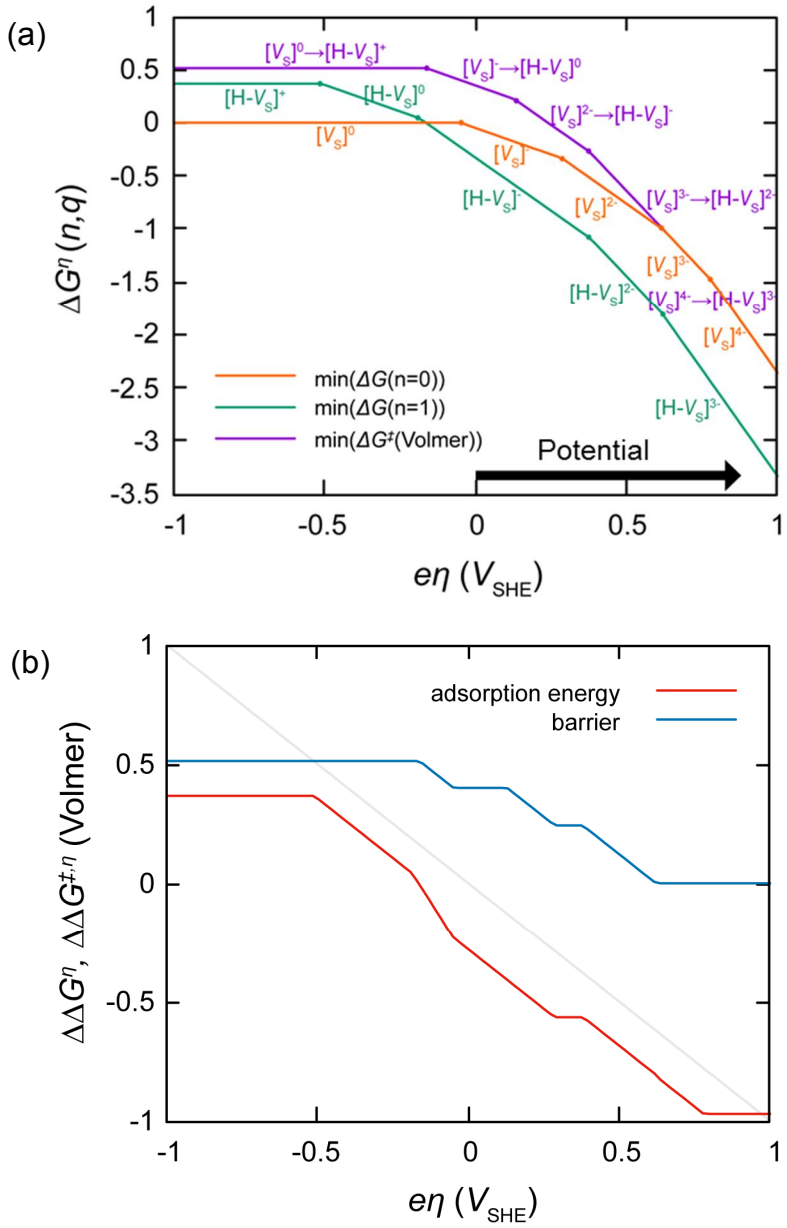

Figure 3.2 (a) State transition diagrams of intermediate and transition states of Volmer step. (b) Minimum adsorption energy and reaction barrier of the Volmer step.

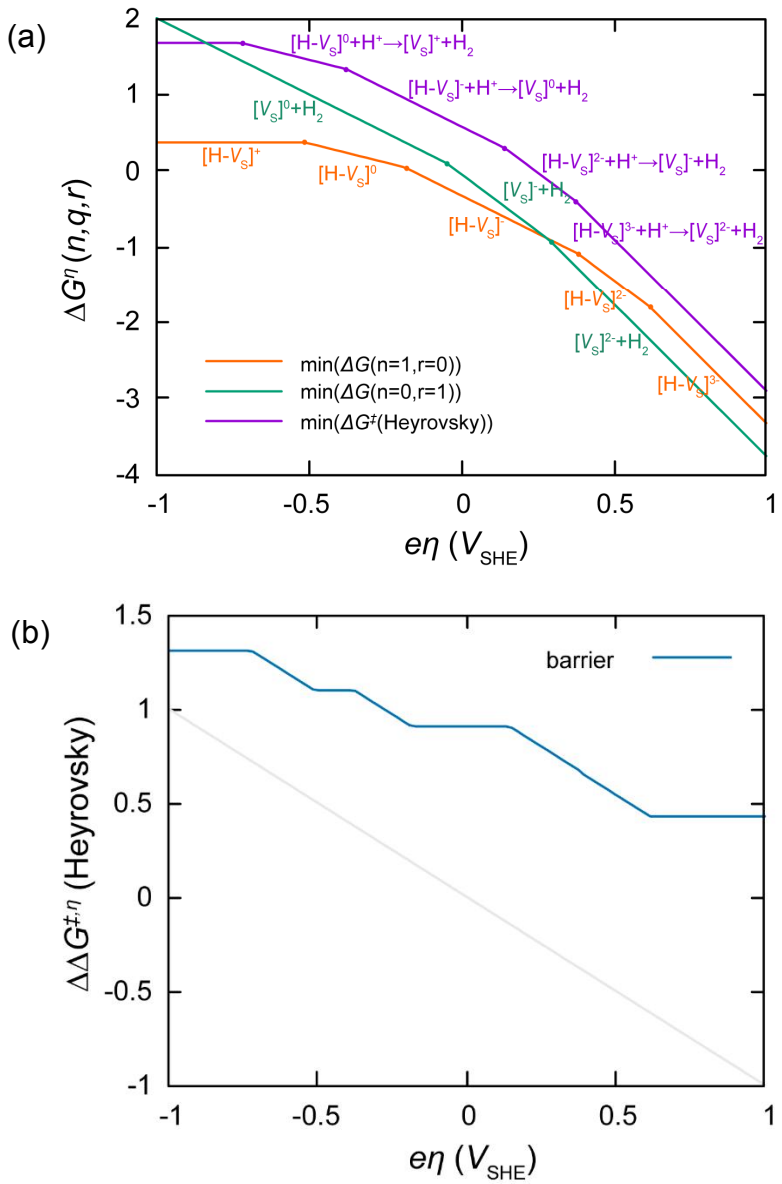

Figure 3.3 (a) State transition diagrams of intermediate and transition states of Heyrovsky step. (b) Minimum reaction barrier of the Heyrovsky step.

3.2.8 Algorithm of KMC

We follow the simple residence-time algorithm.[80] The general algorithm is as follows:[81]

1. Set the time $t = 0$
2. We start from the initial state.
3. Form the list of all N_k possible transition rates at the site r^{ki}, from state k into a generic state i. States that do not communicate with k will have $r^{ki} = 0$.
4. Calculate the cumulative function $R_{ki} = \sum_{j=1}^{i} r_{kj}$ for $i = 1, ..., N_k$. The total rate is $Q_k = R_{k,Nk}$.
5. Get a uniform random number
6. Find the event to carry out i by finding the i for which $R_{k,i-1} < uQ_k \leq R_{ki}$.
7. Carry out event i (update the current state $k \rightarrow i$).
8. Get a new uniform random number $u' \in (0,1]$.
9. Update the time with $t = t + \Delta t$, where $\Delta t = Q_k^{-1} \ln(1/u')$.
10. Return to step 3.

In addition to the above algorithm, we record the history of the states to identify the reaction path. When a desorption event occurs, we reset the history, and when a hydrogen gas is evolved, pile up the recorded history and start another record. In this way, we can define the simplified paths to HER and gather the reaction paths that are essentially same.

Also, before the step 3, we set the charge state of the state to the most stable charge state, because the electronic stabilization is regarded as faster than chemical reactions.

The workflow of our KMC simulation is shown in Figure 3.4. We start from the initial state of $[V_S]^0$. When the current state is $[V_S]^0$ at step 3, delete the history of the state and record chemical and charge state, change the charge state to the most stable state and record. When the chemical state is [H-V_S] or [2H-V_S], update chemical and charge state, change the charge state to the most stable state and update the record. Then, make event table depending on the current state (step 3, 4). The state [V_S] have the events of Volmer step, and the state [H-V_S] have the events of desorption, second Volmer, and Heyrovsky HER. The state [2H-V_S] can have the events of desorption, second Heyrovsky, and Tafel HER. We can select the next event randomly from the event table weighted by rates (step 5, 6). When an event is selected, update history of the state and current state to the final state of the selected event (step 7), then elapse time (step 8, 9), and if the event is a HER, update the number of H_2 evolution and pile the reaction path. We return to step 3 and repeat until if enough HER occurs in KMC simulation to obtain macroscopic measures. When we stop the simulation, we obtain the results of state change over time, the turnover frequency of HER, statistics on reaction paths and so on.

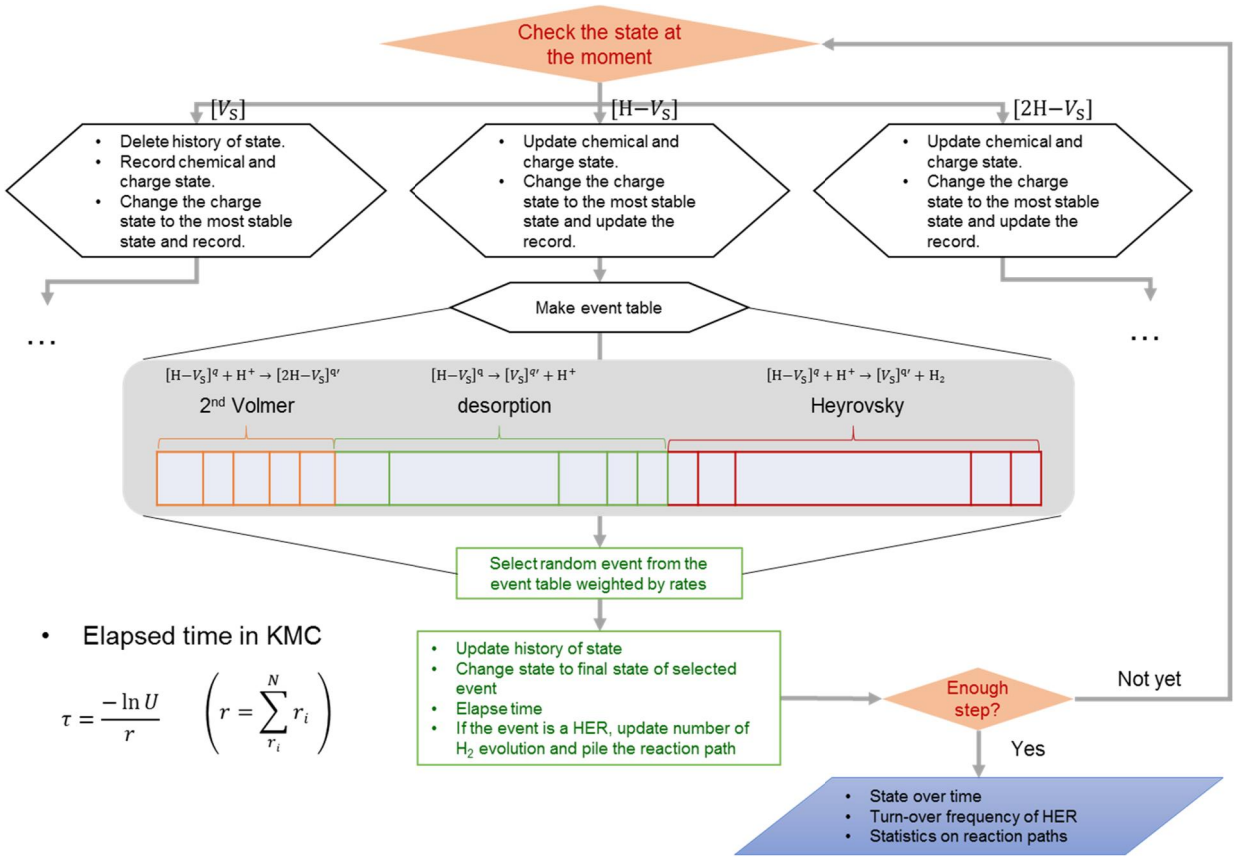

Figure 3.4 Flow chart of our KMC simulation

3.2.7.1 Rate of event

Since we can say that electron transfer is much faster than the chemical reaction steps, the most stable charge state is only considered for the initial state of each elementary step. On the other hand, we consider all possible charge states as the final state; we only have to consider corresponding energy barriers for evaluating reaction rate.

3.2.7.1.1 Reaction barrier

We consider tunneling effect on protonation step (Volmer, Heyrovsky) by scaling the barrier to 80 %[82,83]. Besides, for evaluating the rate of event where the electron is involved, we can assume that the charging event occurs first. In this case, the overall barrier of the step involves charging energy. (See Figure 3.5) This can be proved as follows.

We consider simple energy space like in Figure 3.5. The rate of reaction from A to B, r_{AB}, is much faster than that of reaction from B to C, r_{BC}. It can be seen in the difference of prefactors. The rate of A to B r_{AB} is $F\exp\left(-\frac{(E_a - E_A)}{k_B T}\right)$, and $r_{BC} = f\exp\left(-\frac{(E_b - E_B)}{k_B T}\right)$, where $F >> f$.

r_{BA} and r_{CB} are as the same way: $r_{BA} = F\exp\left(-\frac{(E_a - E_B)}{k_B T}\right)$, and $r_{CB} = f\exp\left(-\frac{(E_b - E_C)}{k_B T}\right)$.

In the steady state, the Boltzmann distribution between two charge states is achieved. Flow from A to B and from B to A are same because the population of state A has to be steady.

$$P_{\mathrm{A}} r_{\mathrm{AB}} = P_{\mathrm{B}} r_{\mathrm{BA}}\,, \tag{3.10}$$

where P_{st} is the population of state *st*. Then, when we define the rate of overall reaction from A to C, following equation comes by considering inflow in state C.

$$P_{\mathrm{A}} r_{\mathrm{AC}} = P_{\mathrm{B}} r_{\mathrm{BC}}\,. \tag{3.11}$$

We combined Eq.(3.10) and Eq.(3.11), and obtain:

$$\begin{aligned} r_{\mathrm{AC}} = \frac{P_{\mathrm{B}} r_{\mathrm{BC}}}{P_{\mathrm{A}}} = \frac{r_{\mathrm{AB}} r_{\mathrm{BC}}}{r_{\mathrm{BA}}} &= \frac{F \exp\left(-\dfrac{(E_{\mathrm{a}} - E_{\mathrm{A}})}{k_{\mathrm{B}} T} \right) \cdot f \exp\left(-\dfrac{(E_{\mathrm{b}} - E_{\mathrm{B}})}{k_{\mathrm{B}} T} \right)}{F \exp\left(-\dfrac{(E_{\mathrm{a}} - E_{\mathrm{B}})}{k_{\mathrm{B}} T} \right)} \\ &= f \exp\left(-\frac{(E_b - E_{\mathrm{A}})}{k_{\mathrm{B}} T} \right) \end{aligned} \tag{3.12}$$

We can just consider the transition state of the rate-determining reaction, the chemical reaction, and electronic charging energy is just included in the barrier. (See Figure 3.6)

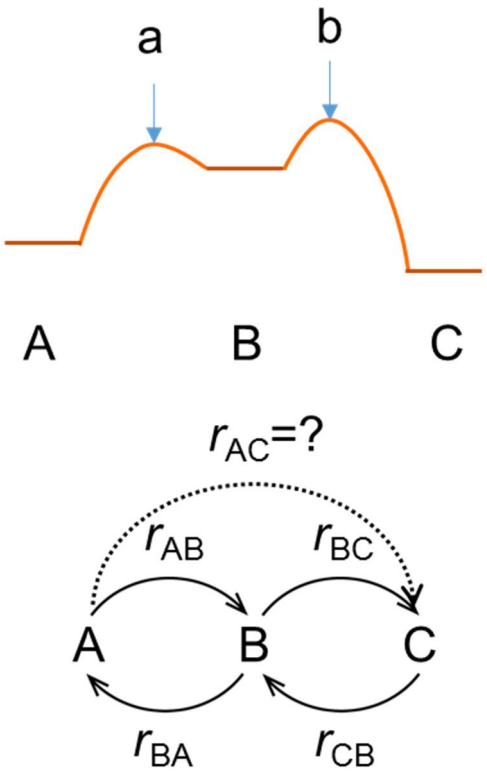

Figure 3.5 Schematic model for the proof for overall reaction rate including fast charging event.

3.2.7.1.2 Pre-exponential factors of rates

Adsorption rate can be defined by multiplying local sticking coefficient and a factor representing the activity of the adsorbing element[84].

$$r_i^{\mathrm{ad}}(T, p_i) = \tilde{S}_i(T) \frac{p_i A_{uc}}{\quad}, \tag{3.13}$$

here $\tilde{S}_i(T)$ is the local sticking coefficient which is comprised of exponential term:

$$\tilde{S}_i(T) = f_i^{\mathrm{ad}}(T) \left(\frac{A_i}{\quad}\right) \exp\left(-\frac{0.8 \cdot \Delta\Delta^{\ddagger}G_i}{\quad}\right), \tag{3.14}$$

where the factor f_i^{ad} accounts for a further reduction in the sticking probability. An accurate determination of the factor would require computationally highly demanding dynamical simulations of a statistically relevant number of trajectories for the impinging molecules, but here we can just approximate the factor as 1. $\frac{A_i}{A_{uc}}$ is the ratio of effective area and the value is $\frac{1}{2}$. Rate enhancement over T is slower than simple thermally activated reaction which follows Arrhenius equation.

Desorption rate can be determined by following formula.

$$\frac{r_i^{\mathrm{ad}}(T, p_i)}{r_i^{\mathrm{des}}(T)} \tag{3.15}$$

For the rate of Heyrovsky and Tafel step, we use the pre-exponential factor of $\frac{k_B T}{h}$, which is an approximation taken from the rate constant

of the dissociation of a hydrogen molecule,[76] where k_B is the Boltzmann constant, h is the Planck constant, T is thermodynamic temperature.

$$r^{\text{Hey.}}(T) = \frac{k_B T}{} \exp\left(-\frac{0.8 \cdot \Delta\Delta^{\ddagger}G^{\text{Hey.}}}{}\right) \tag{3.16}$$

$$r^{\text{Tafel}}(T) - \frac{k_B T}{} \exp\left(-\frac{\Delta\Delta^{\ddagger}G^{\text{Tafel}}}{}\right) \tag{3.17}$$

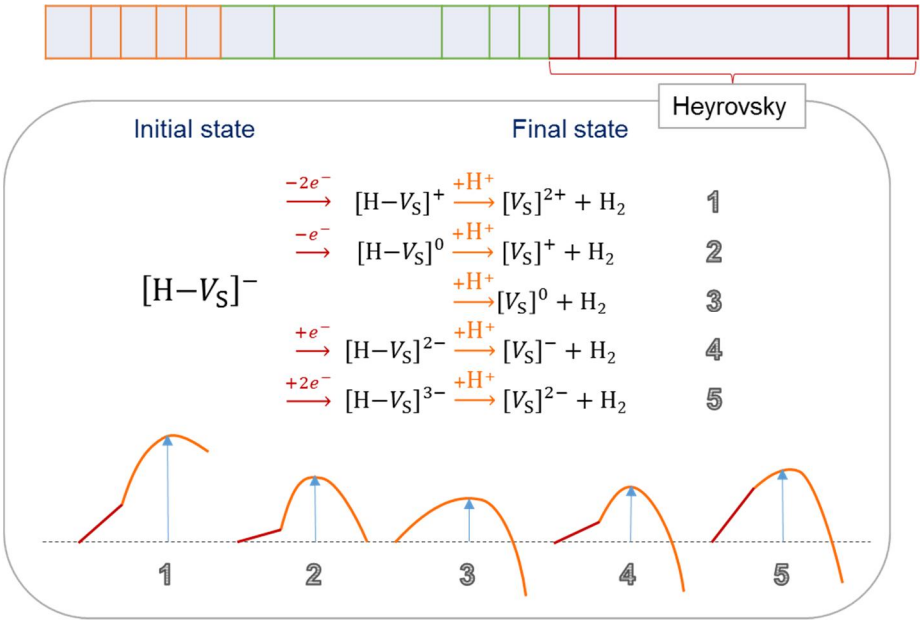

Figure 3.6 Schematic event table weighted by rate and the example of a Heyrovsky step and the relevant energy barriers.

3.3 Result and discussion

We obtain the results of state change over time, the turnover frequency of HER, statistics on reaction paths and so on.

3.3.1 State change over time and turnover frequency

We assume the vacancy is isolated and the interaction between sites are not considered so that we only have to trace one site. The state change of a vacancy site over time is shown in Figure 3.7. The green line in the Figure 3.7b indicates [H-V_S] state and purple line in Figure 3.7a,b indicates a total number of H_2 evolution at the site. Desorption or Heyrovsky step occurs on the time scale of seconds. In the case of desorption, the number of [H-V_S] state, the green data change from 1 to 0 and the number of total H_2 evolution, the purple value doesn't change, and in the case of Heyrovsky step, the total number of H_2 evolution value also changes from n to n+1. Most of the time, the site is maintaining the state of [H-V_S], and [2H-V_S] state does not appear.

Turnover frequency (TOF) of H_2 evolution on sulfur vacancy site of MoS_2 is calculated as 1.78 site^{-1}sec^{-1}, and the exchange current density from the TOF is calculated as 0.018 mA/cm^2 by the following equation.

$$j = 2eN \times \mathrm{TOF}, \tag{3.18}$$

where elementary charge constant $e = 1.6 \times 10^{-19}$ C, and N is the density of sulfur vacancy that we set to the low density of sulfur vacancy, 1.38 %. By tracing the state of the site in time elapsing, we can predict

the population of each state in the sufficiently large catalytic surface with sulfur vacancies. The proportion of the population of each state in the zero biased pH = 0 case is as follows.

$$P([V_S]^q) = 0.00$$

$$P\left([\text{H-}V_S]^q\right) = 1.00 \qquad (3.19)$$

$$P\left([\text{2H-}V_S]^q\right) = 0.00$$

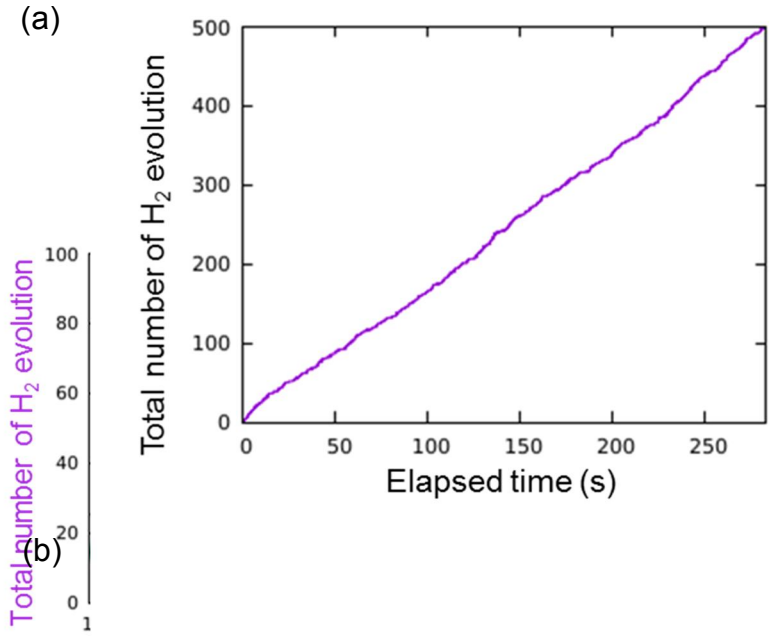

Figure 3.7 State change over time. Green data indicates [H-V_S], and purple data indicates a number of H_2 evolution, respectively.

3.3.2 Reaction mechanism

We trace the pathway through which each HER occurs. Figure 3.8a shows the proportion of each individual HER path. Figure 3.8b,c is the first and second dominant pathway. Both paths are the Volmer-Heyrovsky mechanism, and the rate limiting step is the Heyrovsky step. Two paths differ by whether the charging event occurs before or after the Heyrovsky. The most dominant path is where the charging occurs after the Heyrovsky step due to its lower energy barrier that starts from $[\text{H-}V_S]^{1-}$ state. The first dominant pathway of HER occurs through reduction-protonation-reduction-protonation, and in the second dominant pathway, HER occurs by the sequence of protonation-reduction-reduction-protonation.

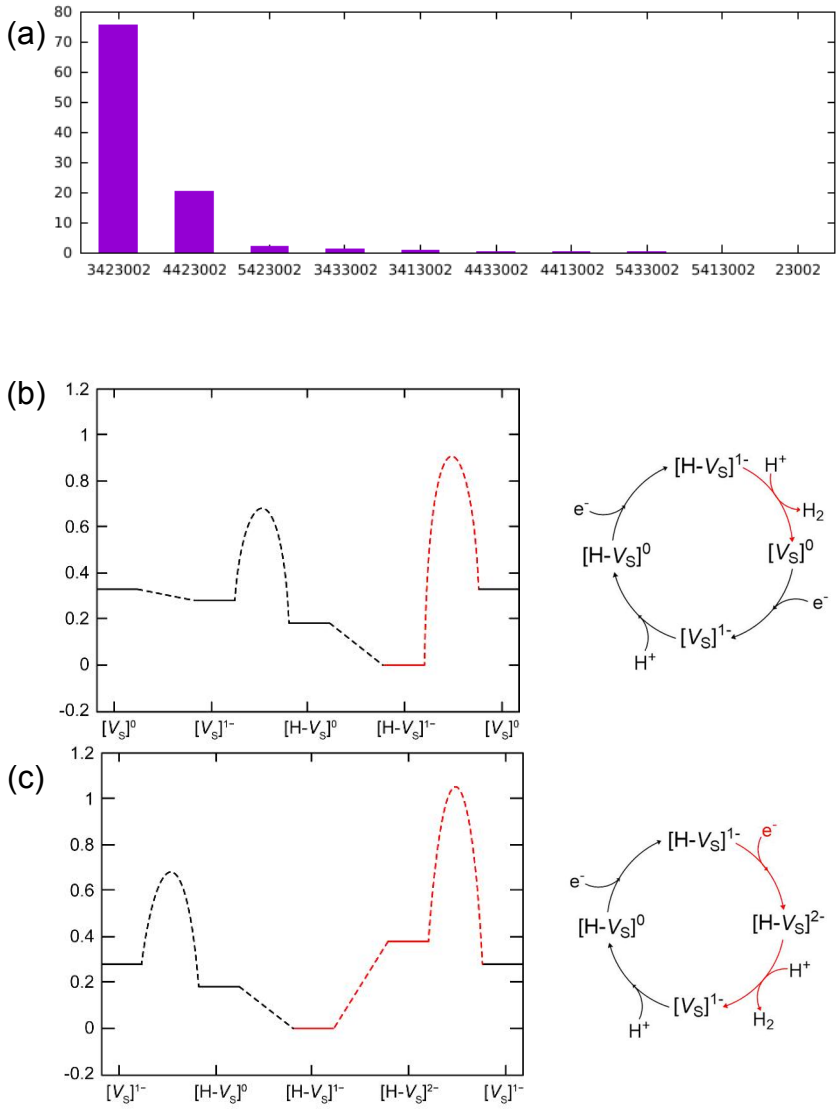

Figure 3.8 (a) Reaction paths and their proportions. (b) Most dominant reaction path. (c) Second dominant reaction path.

3.3.3 Bias dependence

TOF increases with increasing negative bias because barriers decrease. (See Figure 3.2) The population of each state also changes depending on the external bias as shown in Figure 3.9. Plot of exchange current density vs bias is called as polarization curve (Figure 3.10), and the barrier at 10 mA/cm^2 of exchange current density is usually called as overpotential, and our calculated value is 0.335 V. At the point, energy barrier of Heyrovsky step is about 0.7 eV which is ~27 times of k_BT at room temperature, even though we consider tunneling effect that effective barrier is somewhat lowered. In some past studies, simple approach that pays attention to the bias that makes all the thermodynamic reaction energy zero is used, and in that approach, they consider the bias as overpotential. However, from our observation on KMC results of HER on strained and unstrained V_S, HER reaction energy is not important because the Heyrovsky step is the final step of the HER that there cannot be the reverse reaction, but the bias that makes Heyrovsky barrier to certain value (in our approach with tunneling, 0.7 eV) yields 10 mA/cm^2 of exchange current density, which is generally considered to be the overpotential.

In a recent study,[1] overpotential for the MoS_2 system with 12.5 % vacancy is reported as 0.25 V, which is close to our simulation result. We also provide Tafel plot in Figure 3.11 where the external bias with respect to the logarithm of exchange current density is shown. We can resolve Tafel plot by a mechanism to a mechanism. As negative bias increases, dominant mechanism changes and more negatively charged

states lead HER. Energies that is needed to charge the defects negatively decrease with increasing negative bias, and it leads to a reaction path with a lower energy barrier. If active site density increases, Tafel plot is shifted to the right with same Tafel slope.

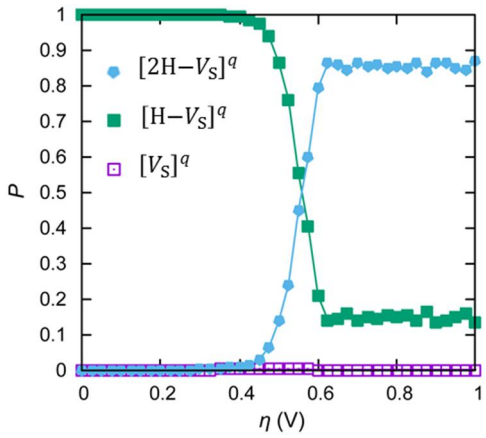

Figure 3.9 Population of each state.

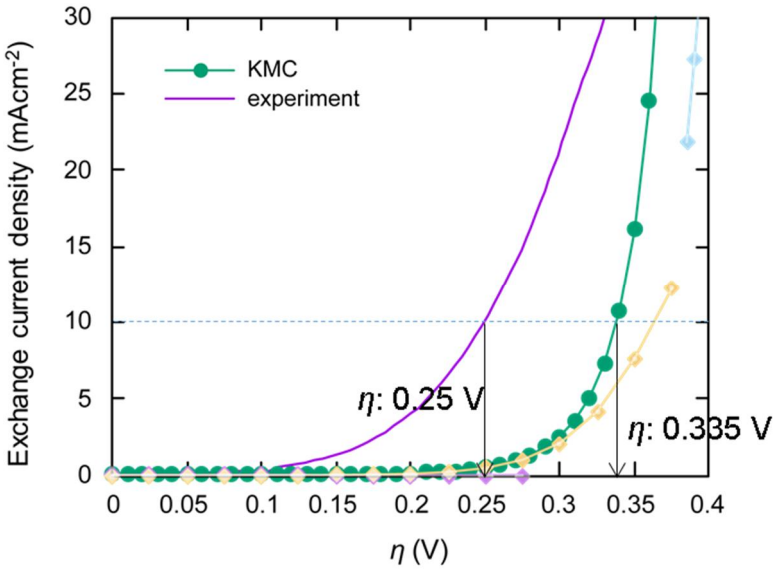

Figure 3.10 Polarization curves from our KMC simulation, and from the experiment.[1]

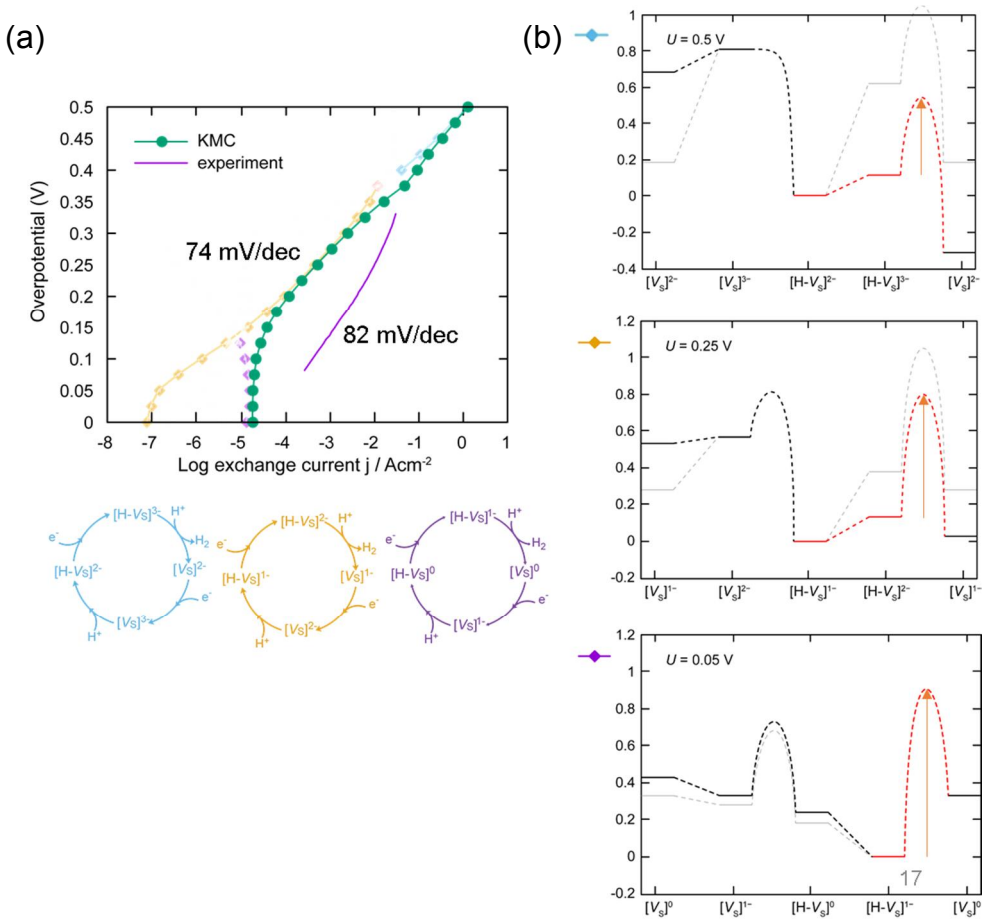

Figure 3.11 (a) Tafel plot resolved by the mechanism. (b) Three representative dominant mechanisms depending on the external bias.

3.3.4 Simple model

On the basis of the observation on KMC results, we have developed a simple model for the TOF of HER on V_S in MoS_2. The resultant predictions are in good agreement with the KMC results. The ability to predict TOF of HER can be widely used to design a novel catalyst from the first-principles calculation results.

$$
\begin{aligned}
&\mathrm{TOF} = \\
&P([V_S]) \cdot \\
&\min\left(\sum_i^{\mathrm{Volmer}} r_i,\ \sum_i^{\mathrm{Heyrovsky}} r_i + \right. \\
&\qquad \left. \min\left(\sum_i^{2^{\mathrm{nd}}\,\mathrm{Volmer}} r_i,\ \sum_i^{2^{\mathrm{nd}}\,\mathrm{Heyrovsky\ Tafel}} r_i\right)\right) \\
&+P([\mathrm{H}\text{-}V_S]) \cdot \left(\sum_i^{\mathrm{Heyrovsky}} r_i + \min\left(\sum_i^{2^{\mathrm{nd}}\,\mathrm{Volmer}} r_i,\ \sum_i^{2^{\mathrm{nd}}\,\mathrm{Heyrovsky\ Tafel}} r_i\right)\right) \\
&+P([2\mathrm{H}\text{-}V_S]) \cdot \left(\sum_i^{2^{\mathrm{nd}}\,\mathrm{Heyrovsky\ Tafel}} r_i\right)
\end{aligned}
\tag{3.20}
$$

Populations in the formula above are obtained by the rates as follows because populations at steady state keep the same inflow and outflow:

$$
\begin{aligned}
&P(V_S)\cdot r^{\mathrm{ad}} = P(\mathrm{H}\text{-}V_S)\left(r^{\mathrm{des}} + r^{\mathrm{Hey}}\right) + P(2\mathrm{H}\text{-}V_S)\cdot r^{\mathrm{Tafel}} \\
&P(\mathrm{H}\text{-}V_S)\left(r^{\mathrm{des}} + r^{\mathrm{Hey}} + r^{\mathrm{ad(2)}}\right) = P(V_S)\cdot r^{\mathrm{ad}} + P(2\mathrm{H}\text{-}V_S)\left(r^{\mathrm{des(2)}} + r^{\mathrm{Hey(2)}}\right) \\
&P(2\mathrm{H}\text{-}V_S)\left(r^{\mathrm{des(2)}} + r^{\mathrm{Hey(2)}} + r^{\mathrm{Tafel}}\right) = P(\mathrm{H}\text{-}V_S)\cdot r^{\mathrm{ad(2)}} \\
&P(V_S) + P(\mathrm{H}\text{-}V_S) + P(2\mathrm{H}\text{-}V_S) = 1
\end{aligned}
\tag{3.21}
$$

The results from this simple model are consistent with macroscopic measures of KMC simulation.

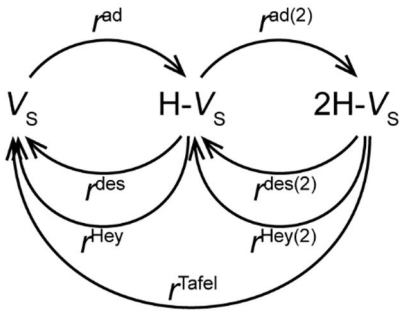

3.3.5 Strain effect

We also examine the strain effect by using the additional data set of DFT calculation about the system with applied strain. (Table 3.2, 3.3) When a tensile strain is applied to MoS_2, negatively charging energies of defects decrease (green dotted circle in Figure 3.12), and it leads to reaction paths with lower energy barriers. Estimating quantitative enhancement of the activity by applying strain using a descriptor of hydrogen binding energy is failed in the previous study.[1] (0.01 eV of hydrogen binding energy difference and 0.08 eV of the overpotential change differ by one order of magnitude.) Here, we could successively estimate the strain effect, quantitatively.

Table 3.2 All calculation data when 2.7 % of compressive strain is applied. Kim (2016)[2]

$2H^+ + 2e^- \xrightarrow{\Delta G_{HER}} H_2$ $\quad \varepsilon = -2.7\ \%$

$\Delta G_{HER} = -2e\eta + 0.1182pH$ $\quad$ at $pH = 0$

Step	Reaction formula $[nH{-}V_S]^q + mH^+ \rightarrow [n'H{-}V_S]^{q'} + rH_2$	$\Delta G^\eta(n,q)$ (eV)	$\Delta G^\eta(n',q') + r\Delta G^\eta_{HER}$ (eV)	$\Delta\Delta G^\ddagger$ (eV)
Volmer	$[V_S]^0 + H^+ \rightarrow [H{-}V_S]^+$	0.000	0.337	0.565
	$[V_S]^- + H^+ \rightarrow [H{-}V_S]^0$	$0.116 - e\eta$	$-0.025 - e\eta$	0.391
	$[V_S]^{2-} + H^+ \rightarrow [H{-}V_S]^-$	$0.613 - 2e\eta$	$-0.036 - 2e\eta$	0.191
	$[V_S]^{3-} + H^+ \rightarrow [H{-}V_S]^{2-}$	$1.422 - 3e\eta$	$0.475 - 3e\eta$	0.086
	$[V_S]^{4-} + H^+ \rightarrow [H{-}V_S]^{3-}$	$2.350 - 3e\eta$	$1.244 - 4e\eta$	0.000
2nd Volmer	$[H{-}V_S]^- + H^+ \rightarrow [2H{-}V_S]^0$	$-0.036 - 2e\eta$	$0.384 - 2e\eta$	1.028
	$[H{-}V_S]^{2-} + H^+ \rightarrow [2H{-}V_S]^-$	$0.475 - 3e\eta$	$0.454 - 3e\eta$	0.694
	$[H{-}V_S]^{3-} + H^+ \rightarrow [2H{-}V_S]^{2-}$	$1.244 - 4e\eta$	$0.995 - 4e\eta$	0.408
Heyrovsky	$[H{-}V_S]^+ + H^+ \rightarrow [V_S]^{2+} + H_2$	0.337	2.500	1.298
	$[H{-}V_S]^0 + H^+ \rightarrow [V_S]^+ + H_2$	$-0.025 - e\eta$	$1.170 - e\eta$	0.921
	$[H{-}V_S]^- + H^+ \rightarrow [V_S]^0 + H_2$	$-0.036 - 2e\eta$	$0.000 - 2e\eta$	0.971
	$[H{-}V_S]^{2-} + H^+ \rightarrow [V_S]^- + H_2$	$0.475 - 3e\eta$	$0.116 - 3e\eta$	1.120
	$[H{-}V_S]^{3-} + H^+ \rightarrow [V_S]^{2-} + H_2$	$1.244 - 4e\eta$	$0.613 - 4e\eta$	0.471
2nd Heyrovsky	$[2H{-}V_S]^0 + H^+ \rightarrow [H{-}V_S]^+ + H_2$	$0.384 - 2e\eta$	$0.337 - 2e\eta$	0.916
	$[2H{-}V_S]^- + H^+ \rightarrow [H{-}V_S]^0 + H_2$	$0.454 - 3e\eta$	$-0.025 - 3e\eta$	0.811
	$[2H{-}V_S]^{2-} + H^+ \rightarrow [H{-}V_S]^- + H_2$	$0.995 - 4e\eta$	$-0.036 - 4e\eta$	0.727
Tafel	$[2H{-}V_S]^0 \rightarrow [V_S]^0 + H_2$	$0.384 - 2e\eta$	$0.000 - 2e\eta$	1.318
	$[2H{-}V_S]^- \rightarrow [V_S]^- + H_2$	$0.454 - 3e\eta$	$0.116 - 3e\eta$	1.256
	$[2H{-}V_S]^{2-} \rightarrow [V_S]^{2-} + H_2$	$0.995 - 4e\eta$	$0.613 - 4e\eta$	1.299

Table 3.3 All calculation data when 2.7 % of tensile strain is applied. Kim (2016)[2]

$2\mathrm{H}^+ + 2e^- \xrightarrow{\Delta G_{\mathrm{HER}}} \mathrm{H}_2$ $\quad \varepsilon = +2.7\ \%$

$\Delta G_{\mathrm{HER}} = -2e\eta + 0.1182p\mathrm{H}$ $\quad$ at $p\mathrm{H} = 0$

Step	Reaction formula $[n\mathrm{H}{-}V_\mathrm{S}]^q + m\mathrm{H}^+ \rightarrow [n'\mathrm{H}{-}V_\mathrm{S}]^{q'} + r\mathrm{H}_2$	$\Delta G^\eta(n,q)$ (eV)	$\Delta G^\eta(n',q') + r\Delta G^\eta_{\mathrm{HER}}$ (eV)	$\Delta\Delta G^\ddagger$ (eV)
Volmer	$[V_\mathrm{S}]^0 + \mathrm{H}^+ \rightarrow [\mathrm{H}{-}V_\mathrm{S}]^+$	0.000	0.417	0.609
	$[V_\mathrm{S}]^- + \mathrm{H}^+ \rightarrow [\mathrm{H}{-}V_\mathrm{S}]^0$	$-0.240 - e\eta$	$-0.226 - e\eta$	0.485
	$[V_\mathrm{S}]^{2-} + \mathrm{H}^+ \rightarrow [\mathrm{H}{-}V_\mathrm{S}]^-$	$-0.249 - 2e\eta$	$-0.619 - 2e\eta$	0.314
	$[V_\mathrm{S}]^{3-} + \mathrm{H}^+ \rightarrow [\mathrm{H}{-}V_\mathrm{S}]^{2-}$	$-0.019 - 3e\eta$	$-0.519 - 3e\eta$	0.202
	$[V_\mathrm{S}]^{4-} + \mathrm{H}^+ \rightarrow [\mathrm{H}{-}V_\mathrm{S}]^{3-}$	$0.363 - 3e\eta$	$-0.269 - 4e\eta$	0.000
2nd Volmer	$[\mathrm{H}{-}V_\mathrm{S}]^- + \mathrm{H}^+ \rightarrow [2\mathrm{H}{-}V_\mathrm{S}]^0$	$-0.619 - 2e\eta$	$-0.211 - 2e\eta$	1.024
	$[\mathrm{H}{-}V_\mathrm{S}]^{2-} + \mathrm{H}^+ \rightarrow [2\mathrm{H}{-}V_\mathrm{S}]^-$	$-0.519 - 3e\eta$	$-0.526 - 3e\eta$	0.644
	$[\mathrm{H}{-}V_\mathrm{S}]^{3-} + \mathrm{H}^+ \rightarrow [2\mathrm{H}{-}V_\mathrm{S}]^{2-}$	$-0.269 - 4e\eta$	$-0.430 - 4e\eta$	0.415
Heyrovsky	$[\mathrm{H}{-}V_\mathrm{S}]^+ + \mathrm{H}^+ \rightarrow [V_\mathrm{S}]^{2+} + \mathrm{H}_2$	0.417	2.263	1.217
	$[\mathrm{H}{-}V_\mathrm{S}]^0 + \mathrm{H}^+ \rightarrow [V_\mathrm{S}]^+ + \mathrm{H}_2$	$-0.226 - e\eta$	$1.064 - e\eta$	1.027
	$[\mathrm{H}{-}V_\mathrm{S}]^- + \mathrm{H}^+ \rightarrow [V_\mathrm{S}]^0 + \mathrm{H}_2$	$-0.619 - 2e\eta$	$0.000 - 2e\eta$	0.902
	$[\mathrm{H}{-}V_\mathrm{S}]^{2-} + \mathrm{H}^+ \rightarrow [V_\mathrm{S}]^- + \mathrm{H}_2$	$-0.519 - 3e\eta$	$-0.240 - 3e\eta$	0.695
	$[\mathrm{H}{-}V_\mathrm{S}]^{3-} + \mathrm{H}^+ \rightarrow [V_\mathrm{S}]^{2-} + \mathrm{H}_2$	$-0.269 - 4e\eta$	$-0.249 - 4e\eta$	0.573
2nd Heyrovsky	$[2\mathrm{H}{-}V_\mathrm{S}]^0 + \mathrm{H}^+ \rightarrow [\mathrm{H}{-}V_\mathrm{S}]^+ + \mathrm{H}_2$	$-0.211 - 2e\eta$	$0.417 - 2e\eta$	0.904
	$[2\mathrm{H}{-}V_\mathrm{S}]^- + \mathrm{H}^+ \rightarrow [\mathrm{H}{-}V_\mathrm{S}]^0 + \mathrm{H}_2$	$-0.526 - 3e\eta$	$-0.226 - 3e\eta$	0.822
	$[2\mathrm{H}{-}V_\mathrm{S}]^{2-} + \mathrm{H}^+ \rightarrow [\mathrm{H}{-}V_\mathrm{S}]^- + \mathrm{H}_2$	$-0.430 - 4e\eta$	$-0.619 - 4e\eta$	0.586
Tafel	$[2\mathrm{H}{-}V_\mathrm{S}]^0 \rightarrow [V_\mathrm{S}]^0 + \mathrm{H}_2$	$-0.211 - 2e\eta$	$0.000 - 2e\eta$	1.242
	$[2\mathrm{H}{-}V_\mathrm{S}]^- \rightarrow [V_\mathrm{S}]^- + \mathrm{H}_2$	$-0.526 - 3e\eta$	$-0.240 - 3e\eta$	1.206
	$[2\mathrm{H}{-}V_\mathrm{S}]^{2-} \rightarrow [V_\mathrm{S}]^{2-} + \mathrm{H}_2$	$-0.430 - 4e\eta$	$-0.249 - 4e\eta$	1.298

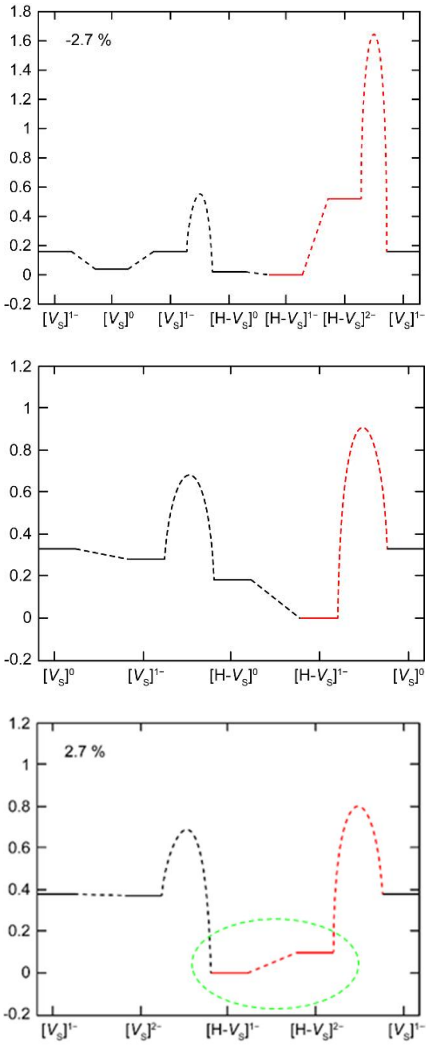

Figure 3.12 Three different dominant mechanisms depending on the applied strain on the system.

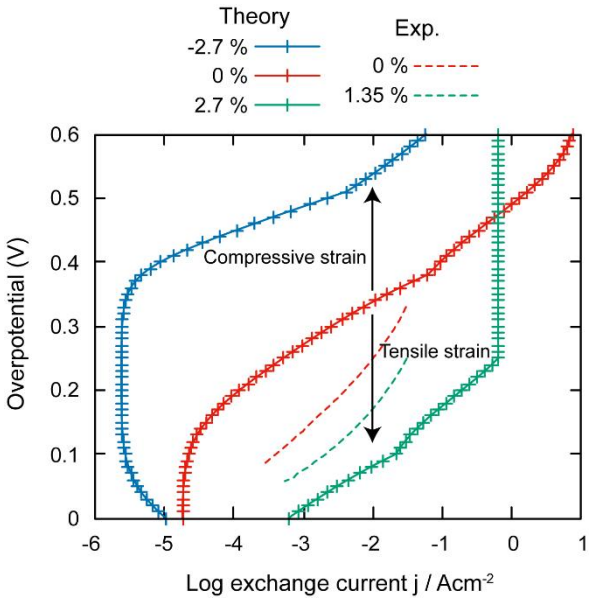

Figure 3.13 Tafel plots of systems with tensile and compressive strain and without strain.

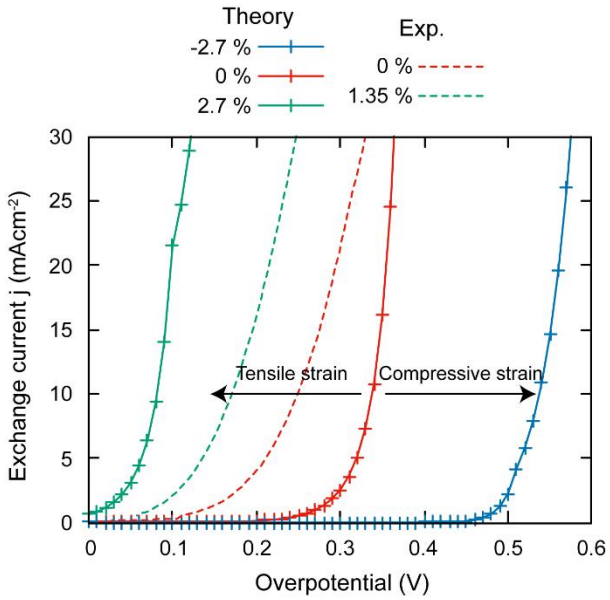

Figure 3.14 Polarization curves of systems with tensile and compressive strain and without strain.

3.4 Summary: mechanisms of HER

In summary, from the DFT calculation and KMC simulation, we show that HER at sulfur vacancy site of MoS_2 are dominated by the Volmer-Heyrovsky mechanism. The rate-determining step is the Heyrovsky step. The energy barrier of Heyrovsky step decreases in the more negatively charged condition of the defect site. By this mechanism, applying bias can facilitate HER. In addition, when a tensile strain is applied to MoS_2, negatively charging energies of defects decrease, and it leads to reaction paths with lower energy barriers.

Chapter 4. Screening active anion vacancy sites of various TMDs for HER

4.1. Introduction: Screening HER catalyst

Hydrogen is a strong contender for a next-generation clean energy source that may replace the current fossil fuels. There are several issues, however, ranging from the hydrogen production and storage to the efficiency of hydrogen fuel cells, which hinders a large-scale hydrogen industry.[5] In particular, the low-cost and clean production of hydrogen source is a critical issue. Currently, fossil fuels are still the main resource for the production of hydrogen due to their low costs and applicability for many fossil fuel-based machines, but the fossil fuels are limited resources and possess the problem of CO_2 and pollutants emission.[5] On the other hand, the hydrogen production by splitting water, the abundant resource on earth, may resolve many of these problems, particularly if it is driven by the solar energy.

To split water using solar energy or electricity, catalysts are necessary to reduce the large overpotential during the hydrogen and oxygen evolution. For several decades, Pt is known to be the best catalyst for hydrogen evolution reaction in water splitting, but the material is very expensive and so might not be suitable for large scale applications. As

such, numerous studies searched for alternative catalysts that have potential to replace Pt.[6–8] Recently, transition metal dichalcogenides (TMDs), most notably MoS_2, are receiving much attention as a catalyst for water splitting because of several advantages such as earth abundance, stability in the acidic media, and its 2D nature where the catalytic active sites might be largely exposed on the surface.[44,57,86] However, the basal plane of many stable TMD phases including MoS_2 is known to be inert. This will disfavor the dissociative adsorption of hydrogen on the TMD surface, which limits HER.[55,56] Although edge sites of some TMD phases are catalytically active,[41,57,87] demands of active basal planes still exist to maximally expose the active sites. In this regard, basal planes of some meta-stable phases such as metallic T-MoS_2 are suggested as an efficient catalytic site,[3,35,58] but for the meta-stable phases, we cannot expect sufficient cyclic properties.

Recently, it was suggested that the basal plane of MoS_2 can also be active in the presence of sulfur vacancies.[1] It was found that the sulfur vacancies in MoS_2 could increase the catalytic activity for HER by enhancing the hydrogen adsorption, and the activity increases even further when the adequate strain was applied on the defective MoS_2. This motivated many researches that introduced vacancies, dopants, and other forms of defects in TMDs for using the material as HER catalysts.[10,37,45,47,59,60] In particular, Voiry *et al* reported largely enhanced HER property for the MoS_2 basal plane by improving electronic coupling with the substrate, and attribute it to activities of naturally occurring sulfur vacancies.[61] This implies that engineering

active sites on the inert basal planes of TMD materials would be possible by introducing anion vacancies.

Therefore, an extensive screening of anion vacancy sites in various TMDs as HER active sites would be critical. In this Letter, we explore the HER efficiencies of basal planes and anion vacancy sites of various TMD materials in terms of calculated hydrogen binding energy on the basis of their volcano relation with experimental catalytic efficiency. To screen proper materials, we searched all stable TMD structures. For the screening targets, we investigate how inert basal plane of TMDs turn to be active with the anion vacancies and suggest four different types of candidate materials that are predicted to have good HER efficiencies depending on the vacancy concentration. In addition, we examine the correlation of some relevant physical quantities with formation energy of the anion vacancy and hydrogen adsorption energy at the anion vacancy sites.

4.2. Computational screening of stable TMDs for HER

4.2.1 Computational detail

Calculations are conducted by density functional theory (DFT) using the Vienna Ab initio Simulation Package (VASP) code[88] based on the projector augmented wave (PAW) pseudopotential[89]. Spin-polarized GGA functional is used for exchange-correlation energy. The cutoff energy for the plane-wave basis set is chosen to be 450 eV, and the k-point mesh grids of 18×18×1 (Monkhorst-Pack) and 4×4×1 are used for 1×1 unitcell and 4×4 supercell, respectively. The ionic configurations are relaxed until the magnitudes of atomic forces of all ions are less than 0.03 eV/Å. For materials having local magnetic moments, which correspond to group 5 TMDs (VS_2, VSe_2, VTe_2, $NbSe_2$, $NbTe_2$, $TaSe_2$ and $TaTe_2$) we assume they are ferromagnetic according to former theoretical studies[90,91]. Although recent DFT study found that antiferromagnetic $TaTe_2$ is more stable than ferromagnetic structure[92], both magnetic configurations are metallic and give similar electronic structures near the Fermi level, so hydrogen binding energies would be similar.

4.2.2 Screening for HER on 40 stable TMD phases

In Figure 4.1a, we list the 40 identified compounds that have stable monolayer TMD structures. They are obtained as follows:

First, we target all the stoichiometric metal dichalcogenides which possibly have quadruply ionized metal, MX_2 (M: metal in group 4~12 and 14, X: chalcogen), since we can assume that chalcogens are doubly negatively ionized in normal condition. From Inorganic Crystal Structure Database (ICSD)[93], we select compounds that exist in layered TMD structures. The compounds that are found only in 3D structures, usually Pyrite structure, or in layered structures with 4-fold coordinated metals such as PdX_2 or GeX_2 (X: S, Se) are excluded from the screening. Second, for each of the selected 40 compounds, we calculate the energy of all monolayer structures in Figure 4.1b to verify phase stability. Then we specified the most stable phase with labels of H, T, T′ and T″ in Figure 4.1a, where H indicates the structure of trigonal prismatic coordination and T is the structure of octahedral coordination; T′ and T″ are distorted T-type structures. Note that, $RhTe_2$ and $AuTe_2$ are excluded at the final step because their stable phases do not belong to 4 structures in Figure 4.1b.

Group 4 TMDs are all found in T phases which agree with experiment [50] and most group 5 TMDs are verified as H phases both in calculation and experiment except monolayer VX_2 have not been reported by experiment[94]. Group 6 TMDs are also primarily found in H phase except for T′-WTe2 which agree with experiment[95]. In group 7 and 9 TMDs, distorted T phases are prevalent, and group 10 TMDs are all stabilized in T phase[50].

The propensity of each TMD for the specific phase can be understood in terms of electron configuration in d shells of transition metals, given

that a trigonal prism of anions is sterically unfavorable than an octahedral coordination so that group 4 metals that have d^0 configurations favor T phase.[50] For instance, group 5 and 6 metals that favor H phase in TMDs have d^1 and d^2 configurations, respectively. Under the crystal field of trigonal prismatic coordination which corresponds to H phase, d orbitals split into three groups, d_{z^2} (a_1), $d_{x^2-y^2,xy}$ (e), and $d_{xz,yz}$ (e') and relatively stable a_1 level can accept one or two d electrons. On the other hand, octahedral coordination in T phases makes d level splitting into $d_{yz,xz,xy}$ (t_{2g}) and d_{z^2,x^2-y^2} (e_g) and stable t_{2g} level can accept up to 6 electrons. When t_{2g} or e_g orbitals are unevenly occupied in T phases, TMDs are often stabilized in distorted T phases as in Group 7 and 9 TMDs due to Jahn-Teller distortions.

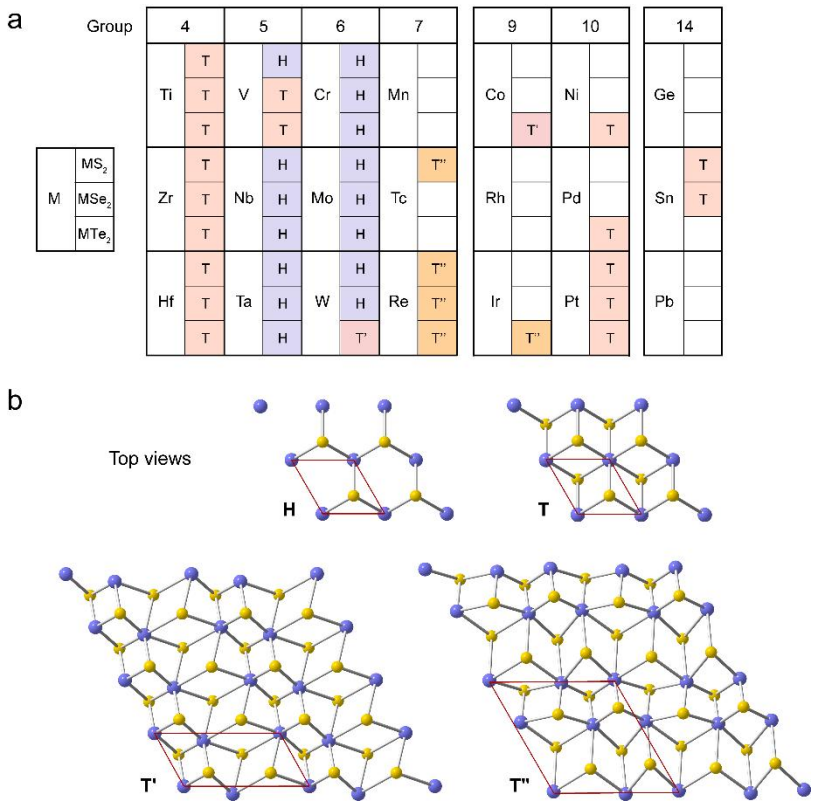

Figure 4.1 Classification of TMD materials. (a) The most stable phases from calculations (b) Searching space of structures to find the most stable phases. H phase is the MoS_2 type which has octahedral coordination. T phase is the CdI_2 type which has trigonal prismatic coordination. T′ and T″ phases are distorted T phases, WTe_2 type, and $ReSe_2$ type, respectively.

4.2.3 Anion vacancy formation

We introduced the anion vacancy in the monolayer TMD. We first introduced one vacancy in the 4×4 supercell, which corresponds to a nominal vacancy density of 3.125 %. However, 3.125 % of vacancy is assumed to be the nearly isolated case, as we confirmed that hydrogen adsorption energies on 3.125 % and 2 % of sulfur vacancies in MoS_2 are same (4×4 supercell and 5×5 supercell were used respectively). The low-symmetry T' and T'' phases have two and four inequivalent adsorption sites, respectively, and we chose the most stable site by comparing vacancy formation energy using 2×2×1 k-point mesh, and for the most stable vacancy site, we obtained converged structure with 4×4×1 k-point mesh.

For the structure of 12.5 % vacancy concentrations, we expanded by 2×2×1 using 2×2×1 supercell with a most stable structure of vacancy. It leads to the uniformly distributed most stable vacancies in 4×4×1 supercell.

We calculate vacancy formation energy from the following equation:

$$E_f^V = E(V_X) - E(\text{clean}) + \mu_X \qquad (4.1)$$

where $E(V_X)$ and $E(\text{clean})$ are energies of the chalcogen vacant cell and clean cell, respectively, and μ_X is the chemical potential of chalcogen *X*. To determine μ_X that reflects relevant in the experimental environment, we consider standard corrosion resistance of *X* assuming that evolution of H_2X gas is equilibrated to 10^{-6} atm at 298.25 K as follows:[70]

$$\mathrm{X}(MX_2) + 2\mathrm{H}^+(\mathrm{aq}) + 2e^- \leftrightarrow \mathrm{H}_2X\ (\mathrm{g}, 10^{-6}\ \mathrm{atm}) \qquad (4.2)$$

$$2\mathrm{H}^{+}(\mathrm{aq}) + 2e^{-} \leftrightarrow \mathrm{H}_2(\mathrm{g}, 1\ \mathrm{atm})\ \text{ at } 0\ V_{\mathrm{RHE}} \qquad (4.3)$$

Then, we define the chemical potential by using the DFT internal energies of H_2X gas phase.

$$\mu_X = E(\mathrm{H}_2X) + k_{\mathrm{B}}T\ln(10^{-6}) - E(\mathrm{H}_2), \qquad (4.4)$$

where $E(\mathrm{H}_2X)$ and $E(\mathrm{H}_2)$ are energies of H_2X and H_2 gas phases, respectively, and T is 298.25 K.

Table 4.1 compiles E_f^V of each TMD, which shows most values lie between 1 and 3 eV.

4.2.4 Hydrogen adsorption free energy

For the selected 40 structures, we calculated hydrogen adsorption free energies to estimate HER efficiency of basal planes and anion vacancy sites in the low and high concentration of vacancy (3.125 % and 12.5 %). The hydrogen adsorption free energy at the potential of $U = 0$ V_{RHE} [87] is calculated as below, where 0 V_{RHE} means zero potential versus the reversible hydrogen electrode:

$$\Delta G_{\mathrm{H}} = \Delta E_{\mathrm{H}} + \Delta\mathrm{ZPE} - T\Delta S, \qquad (4.5)$$

where ΔE_{H} is the hydrogen adsorption energy, ΔZPE is the difference in zero-point energy, T is the temperature (298.25 K) and ΔS is the difference in entropy between H that is adsorbed and in the gas phase, at 1 atm. A normal mode analysis is used to determine the vibrational frequencies of the adsorbed species that determine the zero-point energy and the entropy. $\Delta E_{\mathrm{ZPE}} - T\Delta S$ term of hydrogen adsorption on

MoS_2 V_S was 0.220 eV, and we used the same value for other structures. The hydrogen adsorption energy (ΔE_H) is defined as

$$\Delta E_H = E(*H) - E(*) - \frac{1}{2}E(H_2), \quad (4.6)$$

where E(*H) is the energy of the H adsorbed supercell and E(*) is clean cell energy with active sites.

4.2.5 Hydrogen adsorption on TMD basal plane

For the calculation of hydrogen adsorption energies on the basal planes of TMDs (MX_2), we investigate all possible M top and X top sites to find the most stable adsorption site. Hydrogen is adsorbed mostly on top of chalcogen but on some basal planes such as $NbTe_2$, ReS_2,Se, $TaTe_2$ and etc., hydrogen is adsorbed on top of the metal atoms. To reduce computational costs, we first screen all possible sites using 2×2×1 k-point mesh and further relaxations for the most stable adsorption sites are conducted with 4×4×1 k-point mesh. Within 4 × 4 supercells, further relaxation after removing hydrogen from the hydrogen adsorbed structure sometimes results in new lower-energy phases, but the energy differences (Δ) were less than 0.2 eV/supercell except for $CoTe_2$ and VTe_2 (Δ ~ 0.5 eV), and there is no candidate basal planes even if we consider the newly found phases, thus we used 4 × 4 clean cell energies with no perturbation in Eq. (4.6). We conducted the benchmark comparison for hydrogen adsorption free energy on clean basal planes of TMDs with a previous study[3]. (See Figure 4.2)

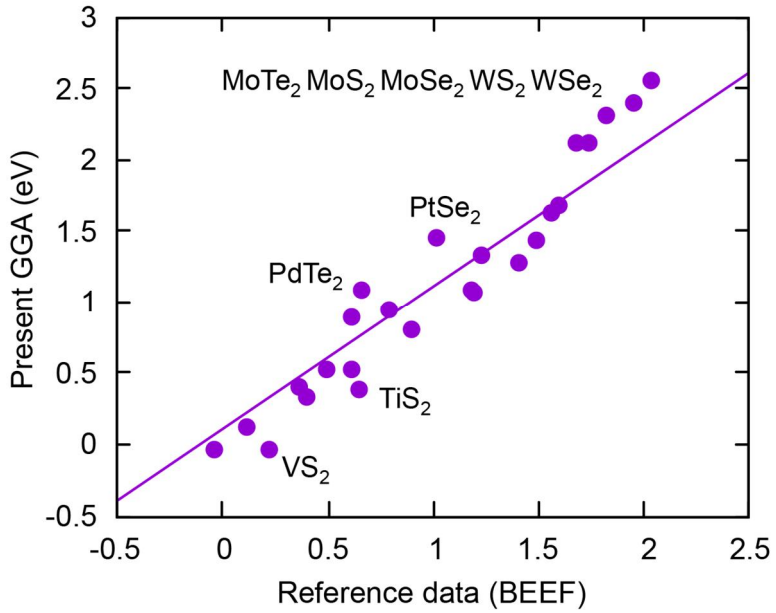

Figure 4.2 Present GGA calculation data vs reference data with BEEF functional[3]. we included data only which the phase and the adsorption site are considered to be the same between two datasets. The differences are not larger than 0.5 eV.

4.2.6 Hydrogen coverage on vacancies of high concentration

4.2.6.1 Equilibrium coverage model

The adsorption of hydrogen can be described with a Frumkin adsorption isotherm[96], an extension of the Langmuir isotherm, by assuming that the Gibbs free energy of hydrogen adsorption is linear with H coverage (θ_{H}).

$$\theta_H = \frac{P_{H_2}^{1/2} e^{-\left(\Delta\Delta G_H^0 + g_H\theta_H\right)/2RT}}{1+P_{H_2}^{1/2} e^{-\left(\Delta\Delta G_H^0 + g_H\theta_H\right)/2RT}} \tag{4.7}$$

In this model, the equilibrium constant is written as follows:

$$K_{\mathrm{H}} = \frac{\theta_{\mathrm{H}}^2}{P_{\mathrm{H}_2}(1-\theta_{\mathrm{H}})^2} = e^{-\left(\Delta G_{\mathrm{H}}^{\circ} + g_{\mathrm{H}}\theta_{\mathrm{H}}\right)/RT}, \tag{4.8}$$

where P_{H_2} is the hydrogen gas pressure – in our case, it is assumed as unity supposing reversible hydrogen electrode (RHE) condition –, $\Delta G_{\mathrm{H}}^{\circ}$ is the Gibbs free energy of hydrogen adsorption at zero hydrogen coverage, and g_{H} is the hydrogen-hydrogen lateral interaction constant.

4.2.6.2 dependence of hydrogen adsorption energy on θ_{H}

For evaluating the assumption of the Frumkin adsorption isotherm that the Gibbs free energy of hydrogen adsorption is linear with θ_{H}, we examine the dependence of hydrogen adsorption energy by varying θ_{H}. The modeling of supercells is shown in Figure 4.3, and the results are shown in Figure 4.4, which shows generally linear dependence.

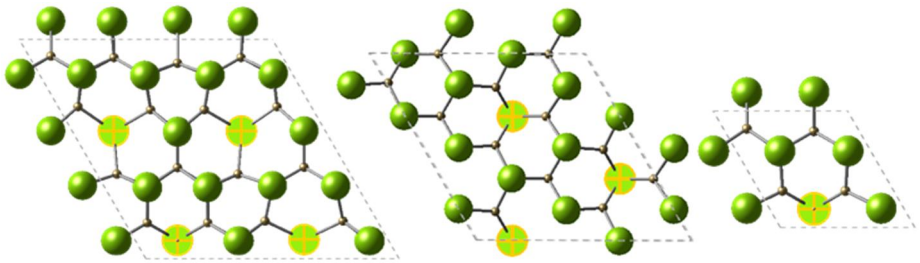

Figure 4.3 Modeling of supercells for examining dependence of hydrogen adsorption energy on θ_H. Using 2×2 supercell with the most stable vacancy, we expand 2×2 or $\sqrt{3}\times\sqrt{3}$ to simulate $\theta_H = \frac{1}{4}$, and $\theta_H = \frac{1}{3}$.

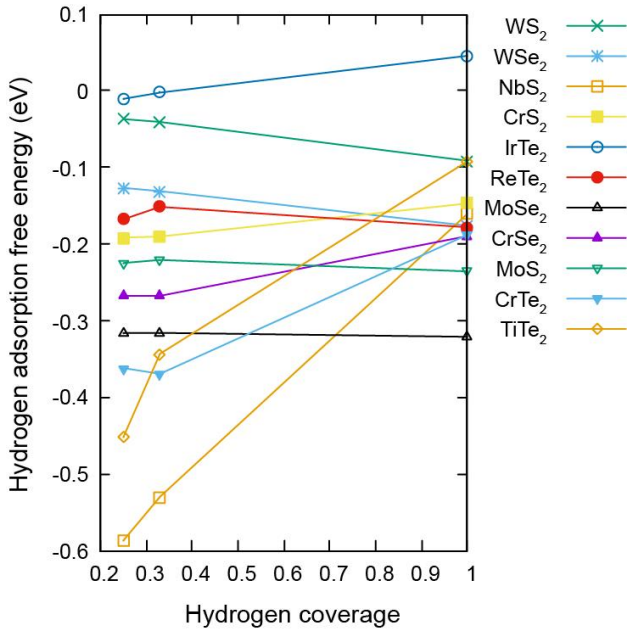

Figure 4.4 Dependence of hydrogen adsorption energy on θ_{H}. It shows generally linear dependence.

4.2.7 Establishing volcano curve

To establish the volcano curves, we calculate the hydrogen adsorption energies on several metal surfaces such as Ni, Co, Pt, Ir, Cu and Au. We compared our results with other studies' data which are obtained using different density functional theory functional with ours. For Ni, Co, Pt, Ir, Cu and Au, we considered face centered cubic phases and (111) surfaces, and hydrogen coverage of 1/9. For Mo which is stable in body-centered cubic, we considered (110) surface and hydrogen coverage of 1/8. The seven-layer slab was used for surface modeling. H adsorbed structure is obtained by relaxing upper two layers of metal atoms only. The most stable adsorption configurations for fcc and bcc phase are checked between the fcc site and top site, or bcc site and top site, respectively. The offset between our data and BEEF reference data is 0.21 eV (see Figure 4.5) and Pt value is at about -0.22 eV on our data. As Pt is the best HER catalyst available today, we aligned the top of volcano curves at Pt level in volcano plots, and we mark shaded region near Pt value ($\Delta G_H^{Pt} - 0.1$ eV $< \Delta G_H < \Delta G_H^{Pt} + 0.1$ eV). If a material lies inside the shaded region, it is assumed as a strong candidate for HER catalyst.

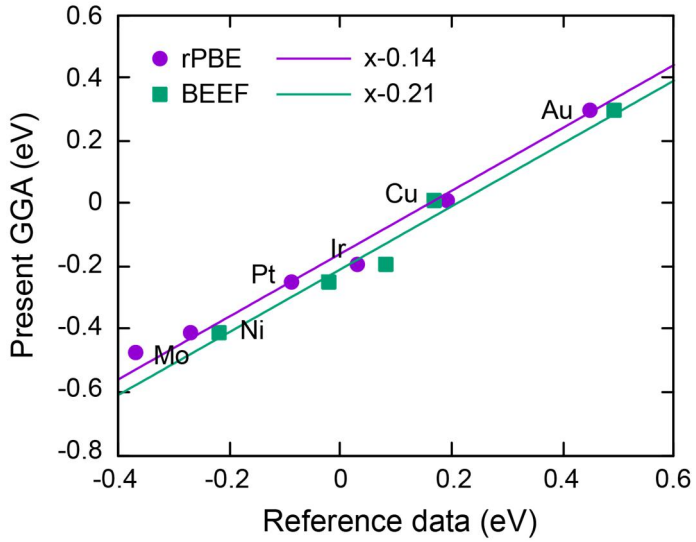

Figure 4.5 Present GGA calculation data vs reference data. Reference data of BEEF functional are from C. Tsai et al., Nano Lett. 14, 1381 (2014)[4]

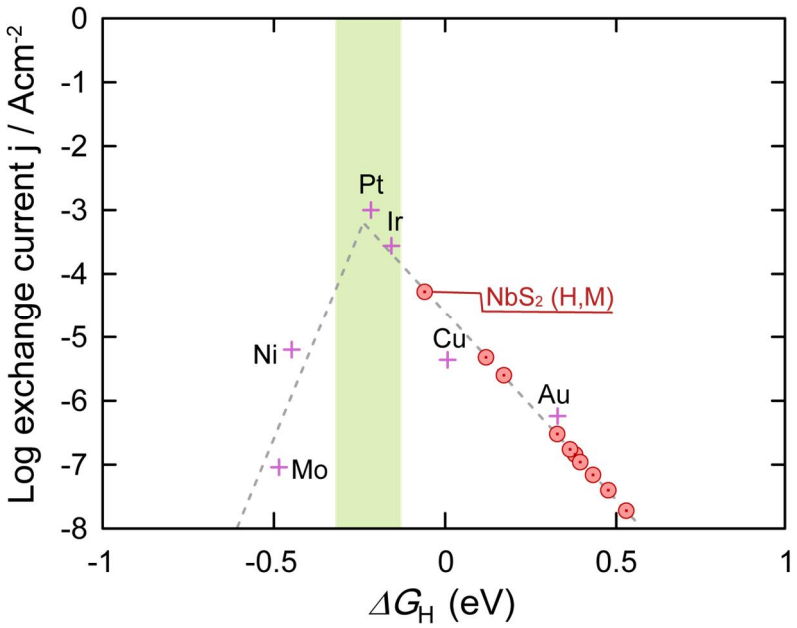

Figure 4.6 Volcano plots of expected HER exchange current as a function of hydrogen adsorption energy for basal planes of TMDs. Shaded region is the range of $\Delta G_H^{Pt} - 0.1$ eV $< \Delta G_H < \Delta G_H^{Pt} + 0.1$ eV.

4.3. Result and discussion

4.3.1 Candidate basal planes of TMD

We plot hydrogen adsorption free energies on the basal planes of TMDs in Figure 4.6 aligning the data on the fitted volcano line obtained from the metal surfaces. However, we found that no strong candidate among basal planes of all TMDs though metallic NbS_2 has the closest value with that of Pt. To understand the factors that determine the H adsorption energy, we investigated electronic structures and found that hydrogen level is hybridized with valence states upon adsorption on the basal planes. When hydrogen atom is adsorbed, the bonding state goes deep in valence band while some part of the valence states has to form anti-bonding states with hydrogen up in the conduction band and the electrons in this states fall into lowest unoccupied molecular orbital (LUMO), i.e. Fermi level in the case of metal or conduction band minimum (CBM) in the case of semiconductor. Therefore, for basal planes, hydrogen adsorption results in relatively large energy gain, especially when LUMO level is high (semiconductors). To make active sites on the basal plane of TMDs, the hydrogen adsorption energy needs to be lowered.

4.3.2 Anion vacancy in TMDs

4.3.2.1 Anion vacancy formation energies in TMDs

In order to understand the variation of vacancy formation energies in the range from 1 to 3 eV, we conduct multiple linear regression with

various bulk properties and the strongest correlations are found with the band gap, formation enthalpy of the phase, and valence level (Figure 4.7). A rough trend is known that the larger band gap the higher vacancy formation energy is.[97] This correlation is stronger in the ionic materials than in the covalent materials. Formation enthalpy of the phase which partially indicates the bond strength is another key parameter affecting vacancy formation energies. The lower the formation enthalpy of the phase, the higher the vacancy formation energy is, due to the phase stability.[97] In addition, we examine a correlation between valence band position relative to the vacuum level and the vacancy formation energy. We assume that the defect level of chalcogen vacant system which has to be occupied in the neutral system is correlated with the valence level. The lower HOMO level of the anion vacant cell can facilitate lower vacancy formation energy.

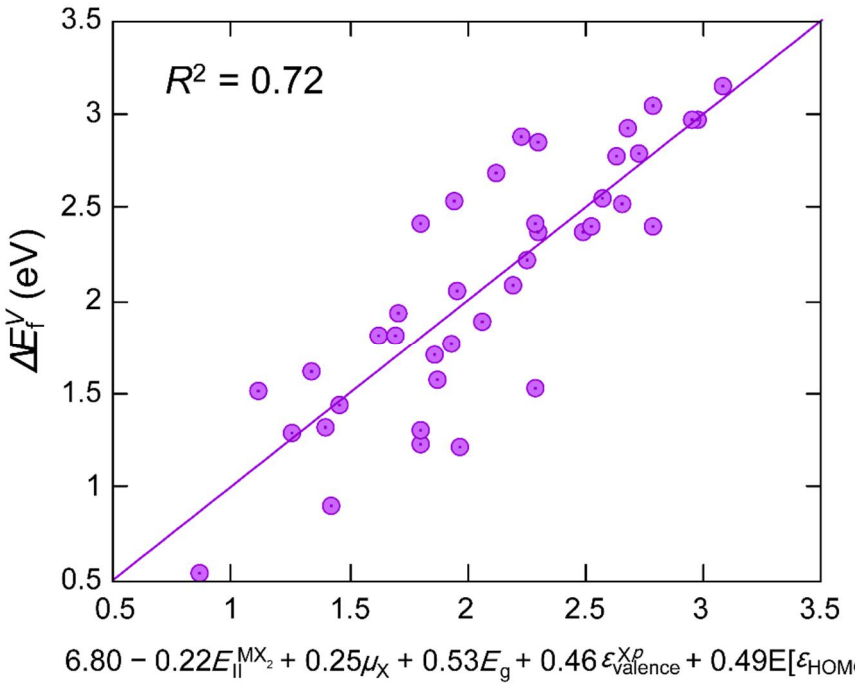

Figure 4.7 Regression result of anion vacancy formation energies in terms of some bulk parameters like ionic interaction energy, band gap, chalcogen p valence level and expected HOMO level. The R^2 score of the regression is 0.72.

4.3.2.2 Electronic structures of TMDs with anion vacancy

In semiconducting TMDs, vacancy induced levels are affecting much on the hydrogen adsorption energies. (See later) Therefore, we investigate the electronic structures of TMDs with chalcogen vacancy in detail and provide a schematic categorization of defect states by Periodic Table group of metals in Figure 4.8. In group 4 TMDs, valence states mostly consist of chalcogen *p* orbitals (up to 75 %) and conduction is mainly composed of metal *d* (~ 85 %), which indicates strong ionic characters of group 4 TMDs. Therefore, the anion vacancies give rise to the shallow donor states and occupied defect level in anion vacant cell lies near CBM[59]. Most group 5 TMDs are metallic and we could not distinguish defect level near Fermi level, so they are omitted from analysis. In group 6 to group 10 TMDs, as the group number increases, the portion of occupied metal *d* states that are hybridized within valence band increases. This strengthens the bonding/antibonding nature of the gap, so the defect levels fall inside the gap as the metal-chalcogen bonds are broken.[59] For these relatively covalent TMDs, the highest occupied defect state lies at low within the gap. For example, a MoS_2 system with sulfur vacancy has the occupied defect level very close to the VBM.

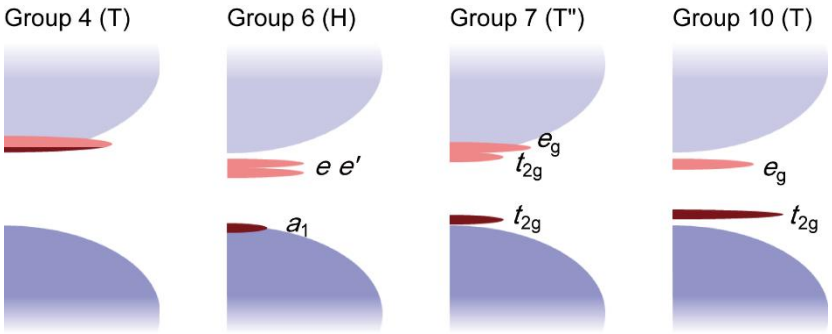

Figure 4.8 Schematic electronic structures of anion vacancy systems classified by a group of the metal atom. Dark color on the bottom part indicates the occupied density of states, and light color on the top part indicates the unoccupied density of states.

4.3.3 Hydrogen adsorption on anion vacancy site in TMD

Next, we calculate hydrogen adsorption energies on vacancy sites of TMDs. We use 4×4×1 supercell (3.125 % of vacancy) to calculate hydrogen adsorption energy on isolated vacancy. On the most stable vacancy sites, we adsorb hydrogen atoms and relax the structures to find the hydrogen adsorbed configurations and calculate the adsorption energies.

Moreover, if we engineer properly, vacancy concentration can be higher albeit thermal stability would be very low. Hydrogen adsorption energies can also be varied as a function of the concentration of vacancy. In order to examine the dependence, we also calculate supercell with a high concentration of anion vacancy (12.5 %). We uniformly distribute vacancies only in the upper layer at the most stable vacancy site found in the 3.125 % configurations. In this case, hydrogen adsorption energies are even coverage dependent. For systems with a high concentration of vacancy, we calculate the hydrogen adsorbed structures with both low coverage ($\theta = 1/4$) and full coverage ($\theta = 1$). For the full coverage, we use the following equation for hydrogen adsorption energy using 4×4×1 supercell to describe hydrogen adsorption and desorption in the full coverage situation[4]:

$$\Delta E_{\mathrm{H}} = E(*n\mathrm{H}) - E(*(n-1)\mathrm{H}) - \frac{1}{2}E(\mathrm{H_2}) \quad (4.9)$$

In fact, hydrogen adsorption energy varies with H coverage, hence we estimate the equilibrium H coverage using the model of Frumkin adsorption isotherm[96,98] in which the adsorption free energy is assumed

to be linear with adsorbate coverage. We find that for the candidates in high vacancy concentration, they all have nearly full H coverage since they have the adsorption free energy below zero. Therefore, we fix coverage to 1 when we show Figure 4.10-11. The calculated data are provided in Table 1.

Table 4.1. Stable phase, band gap, hydrogen adsorption free energy on basal plane, ΔG_H (basal), vacancy formation energy, E_f^V, hydrogen adsorption energy on vacancy site of the system with low vacancy concentration, ΔG_H (H/V), and high vacancy concentration, ΔG_H (4H/4V).

System	Phase (gap in eV)		ΔG_H (basal)	E_f^V	ΔG_H (H/V)	ΔG_H (4H/4V)
$CoTe_2$	T′	metal	0.17	1.34	0.23	0.54
CrS_2	H	0.93	1.33	1.65	0.07	0.00
$CrSe_2$	H	metal	1.63	2.25	-0.03	0.26
$CrTe_2$	H	0.53	1.49	2.79	-0.09	1.23
HfS_2	T	1.28	1.09	2.82	-0.63	-0.59
$HfSe_2$	T	0.58	1.29	2.89	-0.46	-0.41
$HfTe_2$	T	metal	1.02	2.85	-0.32	-0.14
$IrTe_2$	T″	0.63	1.20	2.72	-0.31	0.10
MoS_2	H	1.81	2.11	2.21	0.07	-0.18
$MoSe_2$	H	1.63	2.31	2.64	-0.01	-0.27
$MoTe_2$	H	1.27	2.12	3.10	-0.12	-0.33
NbS_2	H	metal	-0.06	1.12	0.16	0.22
$NbSe_2$	H	metal	0.38	1.64	0.07	0.02
$NbTe_2$	H	metal	0.40	1.93	-0.02	0.16
$NiTe_2$	T	metal	0.74	1.16	0.57	0.61
$PdTe_2$	T	0.34	1.09	1.53	0.56	0.48
PtS_2	T	1.85	1.15	1.28	0.32	0.29
$PtSe_2$	T	1.42	1.46	1.89	0.18	0.16
$PtTe_2$	T	0.81	1.24	2.33	0.09	0.01
ReS_2	T″	1.43	1.44	1.60	0.49	0.20
$ReSe_2$	T″	1.26	1.68	2.24	0.48	-0.30

$ReTe_2$	T″	0.93	1.38	2.92	-0.02	-0.18
SnS_2	T	1.57	0.96	1.35	0.23	0.19
$SnSe_2$	T	0.87	0.76	1.16	0.54	0.29
TaS_2	H	metal	0.12	1.46	0.03	0.18
$TaSe_2$	H	metal	0.48	1.73	0.10	0.12
$TaTe_2$	H	metal	0.37	1.43	0.50	0.27
TcS_2	T″	1.35	0.95	1.08	0.53	0.79
TiS_2	T	metal	0.33	0.68	0.40	0.27
$TiSe_2$	T	metal	0.79	1.54	0.21	0.30
$TiTe_2$	T	metal	0.89	2.36	-0.13	0.17
VS_2	H	metal	0.64	1.07	0.73	0.95
VSe_2	T	metal	0.53	1.33	0.25	0.30
VTe_2	T	metal	0.44	2.08	0.09	0.11
WS_2	H	0.66	2.41	2.37	0.20	-0.07
WSe_2	H	0.58	2.55	2.70	0.14	-0.18
WTe_2	T′	0.14	0.94	2.64	-0.45	-0.51
ZrS_2	T	1.18	0.87	2.25	-0.32	-0.59
$ZrSe_2$	T	0.48	1.08	2.37	-0.20	-0.52
$ZrTe_2$	T	metal	0.99	2.48	-0.18	-0.50

4.3.3.1 Distribution of hydrogen adsorption energies on basal planes and anion vacancy sites

The distribution of hydrogen adsorption energies on basal planes and anion vacancy sites are compared in Figure 4.9. As shown in Figure 4.6, hydrogen adsorption energies on basal planes are distributed away from the value of Pt as they are inert. However, distribution hydrogen adsorption energies on vacancy sites are much shifted to Pt value in both low and high vacancy concentrations. That is, inert semiconducting TMD basal planes get active in HER by inducing anion vacancy and even many metallic TMD materials also become more active than the perfect basal planes. This is because the active localized defect states are involved in the hydrogen adsorption on vacancy site. (See Figure S2) The defect states are less stable than valence states and they can be stabilized by participating in bonding with hydrogen. Especially for semiconducting TMDs, an extra electron can occupy in-gap states, which fills CBM in the case of the basal plane, so much less energy is required to adsorb H atom on anion vacancy sites compared to the basal planes. When we increase the vacancy concentration, the in-gap states are broadened or split and the hydrogen adsorption energies can be changed. Accordingly, the vacancy engineering could be a strong design principle for optimizing inert basal planes as HER catalyst, and by controlling the vacancy concentrations, defect levels can be changed and materials can be further optimized as HER catalysts.

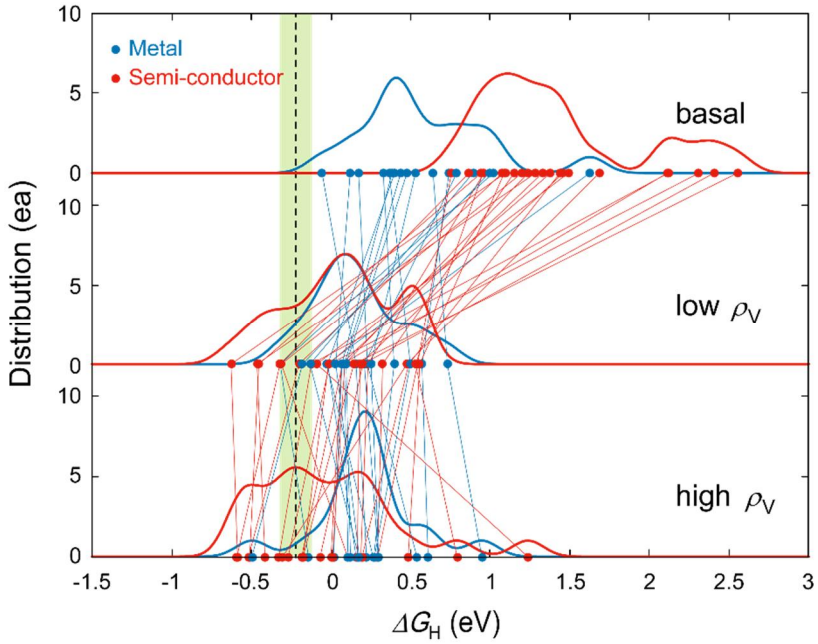

Figure 4.9 Distributions of hydrogen adsorption energies on (a) basal planes of TMDs, (b) anion vacancy sites in systems with low vacancy concentrations and (c) high vacancy concentrations, respectively. Blue points indicate metallic phases and red points are for semiconducting phases. Distributions are obtained from Gauss sums of the points when sigma is set to be 0.1 eV.

4.3.3.2 Candidate TMDs with anion vacancy as an active site

We screen a number of strong candidates (in the shaded region) with the existence of the anion vacancies and plot them following the volcano relation in Figure 5. MoS_2 is not included as a strong candidate in the shade at low concentration of sulfur vacancy (3.125 %), but it becomes one of the strongest candidates when the vacancy concentration is near 12.5 %. Note that the catalytic activities also can be enhanced by inducing strain[1].

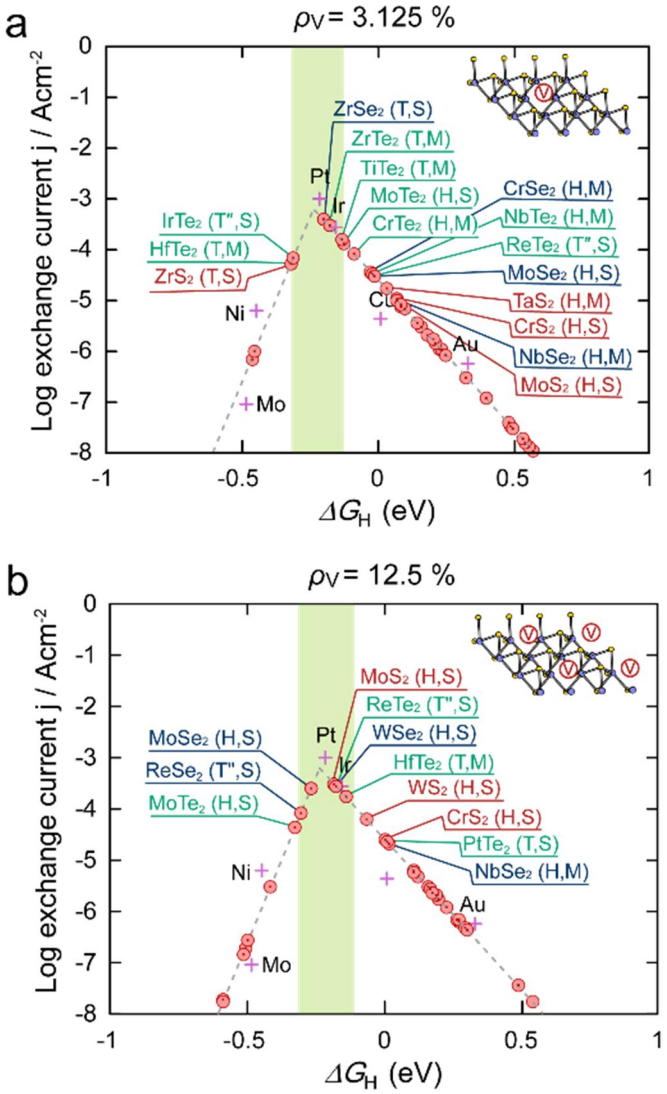

Figure 4.10 Candidate TMDs for HER. Volcano plots for anion vacancy sites of TMDs when the vacancy concentrations are (a) 3.125 % and (b) 12.5 %, respectively.

4.3.3.3 Classification of candidate TMDs with anion vacancy

We classify the candidates in four types according to how the hydrogen binding energy depends on the vacancy density as shown in Figure 4.11. Materials in type I are optimal in high vacancy concentrations rather than relatively inactive low vacancy concentration. Notably, MoS_2 is in this class. Candidates of type III are relevant to the low vacancy concentrations while they get too active when the vacancy concentrations are high. Materials in this class might be unstable when we introduce high concentrations of vacancy[70]. Candidate type II indicate the materials which can be tuned by controlling the vacancy concentrations since the hydrogen adsorption energies at 3.125 % and 12.5 % of vacancy concentrations vary away from Pt value in opposite directions, respectively. Considering known stability issues of TMD tellurides[99], sulfides and selenides attract more attentions. Notably, $MoSe_2$ in type II is expected to be able to be further optimized by fine-tuning the vacancy concentration

Type IV materials show opposite trend with other types. $IrTe_2$ in this type can be tuned by varying vacancy concentration between 3.125 % and 12.5 %. We investigate the reason of opposite trend and found that induced strain by vacancy formation in this material is larger than other materials so the strain controls LUMO level of defective systems. $IrTe_2$ system with a higher concentration of vacancy has higher LUMO level and higher hydrogen adsorption energy. On the other hand, for tellurium vacancy in $HfTe_2$, a hydrogen-unterminated vacancy makes adjacent hydrogen-terminated vacancies more stable by splitting of

hydrogen bonding level with distortion due to the strain. Therefore, when high concentrations of tellurium vacancies are generated in $HfTe_2$ with hydrogen coverage close to 1, hydrogen desorption can be facilitated stabilizing adjacent hydrogen-terminated vacancies.

We can choose candidate materials by type depending on what vacancy concentrations you are assuming. For example, WS_2, WSe_2, and MoS_2 with high vacancy concentration can be the strongest candidates for a high density of active sites.

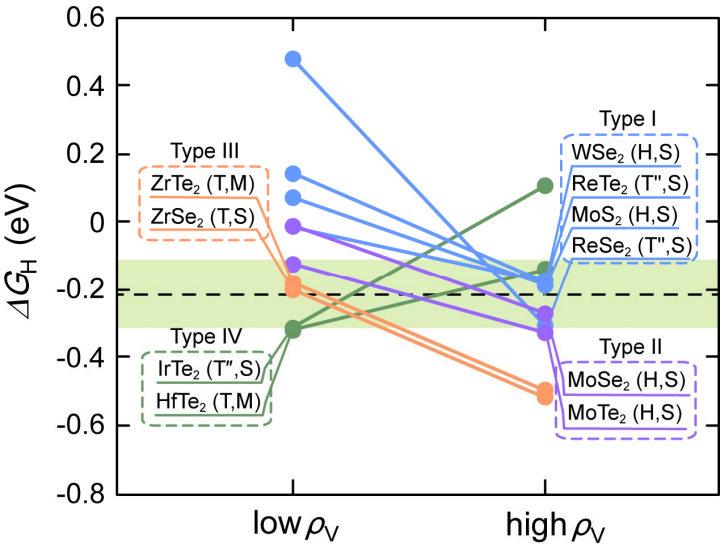

Figure 4.11 Candidate TMDs for HER. The trend of hydrogen adsorption energy as a function of the vacancy concentration. Candidate type I is relevant to the high vacancy concentrations, type II indicates the group of materials which might be optimized by controlling the vacancy concentrations, and type III is relevant to the low vacancy concentrations.

4.3.3.4 Key physical quantities that affect hydrogen adsorption energy

In order to elucidate the enhanced catalytic activities of anion vacancy sites of TMDs, we carry out multiple linear regression. We try to identify the key physical quantities that affect the hydrogen adsorption energy. We use the backward elimination method among various physical quantities from the bulk properties to properties about the anion vacancy. (See Figure 4.12) We find that the hydrogen binding energy on vacancy site is highly correlated with the vacancy formation energy and LUMO level of the vacant system, also somewhat with HOMO level. Localized defect states are already high in energy since the nearest atoms have lost bindings with the anion, and this is reflected in the vacancy formation energy. In hydrogen adsorption, the localized defect states hybridize with hydrogen instead of the vacant anion to form bonding state, the energy that the system has lost in vacancy formation is recovered to some extent. So, the more energy required for vacancy formation, the more hydrogen adsorption is favored on the vacancy site to recover the energy. Also, the excess electron after filling the hydrogen-vacancy bonding state tends to go to LUMO level of the vacant system. So, low LUMO level is the favorable condition for hydrogen adsorption. As for HOMO level, since the bonding state with hydrogen takes two electrons from HOMO level, the high HOMO level is advantageous for adsorption. For an example, if there are occupied defect states such as the a_1 state in MoS_{2-x}, the state forms bonding state with hydrogen and an excess electron goes to the LUMO level, *e* state. (See Figure 4.8)[1]

This is why the vacancy sites are more active than basal planes. As the electrons in the vacant site already have relatively high energy than the valence electrons in a clean system, the site is energetically more active than in the case of basal plane. In addition, in some cases, empty gap states like MoS_{2-x} *e* states form lower LUMO level than CBM, and thus the energy gain aroused from the excess electron can be further lowered. These principles could be applied to suggest another design method which spatially localizes active electrons by some point defects.

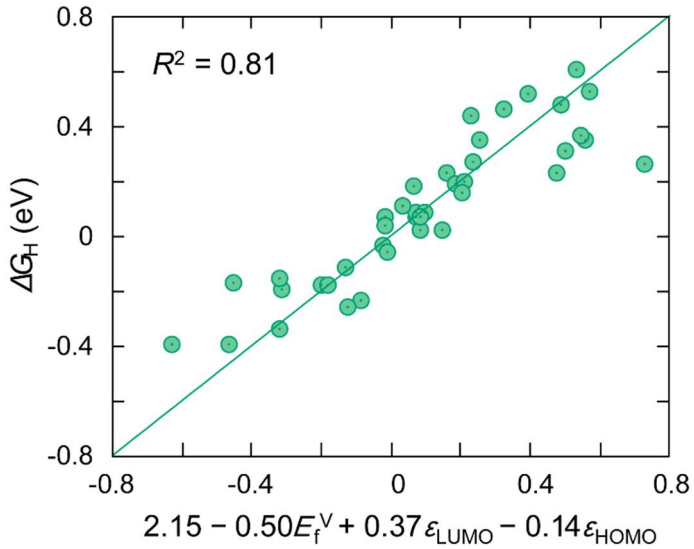

Figure 4.12 Regression result of hydrogen adsorption free energies on anion vacancy sites in terms of vacancy formation energy, LUMO level, and HOMO level. An R^2 score of the regression is 0.86.

4.4. Conclusion: Screening HER catalyst

In conclusion, we have explored the HER efficiencies of basal planes and anion vacancy sites of stable phases of various TMD materials in terms of hydrogen binding energy. Based on the computational results, we suggest that the vacancy control is a strong design principle. Many inert TMD materials become the candidates that may show high catalytic effects in HER by inducing anion vacancies. Moreover, fine-tuning is also possible by engineering vacancy concentrations. Some candidates such as $MoSe_2$ may be tuned to be more efficient between 3.125 % and 12.5 % of vacancy concentration. Note that when the vacancy concentration is ~12.5 %, there are more active sites than edge active sites when flakes of TMD materials have a larger radius than ~ 2 nm, and in this high concentration case, WS_2, WSe_2, and MoS_2 can be the most promising candidates. This largely exposed active sites are an advantage of 2D nature of TMD materials. We expect the candidate materials suggested in this paper to replace Pt and be utilized to the low-cost and clean production of a hydrogen source. Furthermore, we hope this study provides insight into other design principles to make inert 2D materials catalytically active by inducing various kinds of point defects.

4.5. Summary: Screening HER catalyst

We try to find new defective TMD materials for HER catalyst by means of computational screening based on the density functional theory. We explore the HER efficiencies of basal planes and anion vacancy sites for various TMD materials by using the hydrogen binding free energy as the descriptor for the HER exchange current density. We find hydrogen binding energy is varied by the concentration of vacancy and discover good TMD candidates which are expected to show high HER performance in proper vacancy concentrations. We suggest $ZrSe_2$ and $ZrTe_2$ for low vacancy concentration, and $MoSe_2$, $MoTe_2$, WSe_2, $ReTe_2$, MoS_2 and $ReSe_2$ when intermediate or high concentration of vacancy is accessible. We expect for these materials to be able to compete against Pt as HER catalyst without strain engineering. In addition, through multiple linear regression, we identify that the physical quantities related to anion vacancies strongly affect the hydrogen adsorption energy.

Chapter 5. Conclusion

We try to identify the mechanism of HER on sulfur vacancy sites by means of first-principles calculations and kinetic Monte Carlo (KMC) simulation, and we also simulate strain-applied systems. We show that HER at sulfur vacancy site of MoS_2 are dominated by the Volmer-Heyrovsky mechanism. The rate-determining step is the Heyrovsky step. The energy barrier of Heyrovsky step decreases in the more negatively charged condition of the defect site. By this mechanism, applying bias can facilitate HER. In addition, when a tensile strain is applied to MoS_2, negatively charging energies of defects decrease, and it leads to reaction paths with lower energy barriers.

We also try to find new defective TMD materials for HER catalyst by means of computational screening based on the density functional theory. We explore the HER efficiencies of basal planes and anion vacancy sites for various TMD materials by using the hydrogen binding free energy as the descriptor for the HER exchange current density. We find hydrogen binding energy is varied by the concentration of vacancy and discover good TMD candidates which are expected to show high HER performance in proper vacancy concentrations. We suggest $ZrSe_2$ and $ZrTe_2$ for low vacancy concentration, and $MoSe_2$, $MoTe_2$, WSe_2, $ReTe_2$, MoS_2 and $ReSe_2$ when intermediate or high concentration of vacancy is accessible. We expect for these materials to be able to compete against Pt as HER catalyst without strain engineering. In addition, through multiple linear regression, we identify that the

physical quantities related to anion vacancies strongly affect the hydrogen adsorption energy.

As a result, we provide more advanced exploration about HER on anion vacancy sites of various TMDs both in the mechanisms and material screening viewpoints. We believe that the present works can contribute to realizing the rational design of the novel catalysts to replace Pt. Though we confine the screening range in 2D TMDs in this study, our viewpoints could be extended to other novel material systems.

Bibliography

1. Li, H. *et al.* Activating and optimizing MoS2 basal planes for hydrogen evolution through the formation of strained sulphur vacancies. *Nat. Mater.* **15,** 364–364 (2016).

2. Kim, K. Y. Ph . D . DISSERTATION Theoretical investigation on chemical interactions of O 2 and H with defects of MoS 2 monolayer. (Seoul National University, 2017).

3. Pandey, M., Vojvodic, A., Thygesen, K. S. & Jacobsen, K. W. Two-dimensional metal dichalcogenides and oxides for hydrogen evolution: A computational screening approach. *J. Phys. Chem. Lett.* **6,** 1527–1585 (2015).

4. Tsai, C., Abild-Pedersen, F. & Nørskov, J. K. Tuning the MoS_2 Edge-Site Activity for Hydrogen Evolution via Support Interactions. *Nano Lett.* **14,** 1381–1387 (2014).

5. Mazloomi, K. & Gomes, C. Hydrogen as an energy carrier: Prospects and challenges. *Renew. Sustain. Energy Rev.* **16,** 3024–3033 (2012).

6. Du, P. & Eisenberg, R. Catalysts made of earth-abundant elements (Co, Ni, Fe) for water splitting: Recent progress and future challenges. *Energy Environ. Sci.* **5,** 6012 (2012).

7. Liu, Q. *et al.* Carbon nanotubes decorated with CoP nanocrystals: A highly active non-noble-metal nanohybrid electrocatalyst for hydrogen evolution. *Angew. Chemie - Int. Ed.* **53,** 6710–6714 (2014).

8. Popczun, E. J. *et al.* Nanostructured nickel phosphide as an electrocatalyst for the hydrogen evolution reaction. *J. Am. Chem. Soc.* **135,** 9267–9270 (2013).

9. Sim, U. *et al.* N-doped monolayer graphene catalyst on silicon photocathode for hydrogen production. *Energy Environ. Sci.* **6,** 3658 (2013).

10. Ma, L. *et al.* Cobalt-doped edge-rich MoS2/nitrogenated graphene composite as an electrocatalyst for hydrogen evolution reaction. *Mater. Sci. Eng. B Solid-State Mater. Adv. Technol.* **212,** 30–38 (2016).

11. Lebègue, S., Björkman, T., Klintenberg, M., Nieminen, R. M. & Eriksson, O. Two-dimensional materials from data filtering and Ab Initio calculations. *Phys. Rev. X* **3,** 1–7 (2013).

12. Shin, H., Ha, Y. & Kim, H. 2D Covalent Metals: A New Materials Domain of Electrochemical CO2 Conversion with Broken Scaling Relationship. *J. Phys. Chem. Lett.* **7,** 4124–4129 (2016).

13. Koski, K. J. & Cui, Y. The new skinny in two-dimensional nanomaterials. *ACS Nano* **7,** 3739–3743 (2013).

14. Wang, R. *et al.* Ultrafast and spatially resolved studies of charge carriers in atomically thin molybdenum disulfide. *Phys. Rev. B - Condens. Matter Mater. Phys.* **86,** 1–5 (2012).

15. Qi, Y. *et al.* CO2-Induced Phase Engineering: Protocol for Enhanced Photoelectrocatalytic Performance of 2D MoS2 Nanosheets. *ACS Nano* **10,** 2903–2909 (2016).

16. Das, S., Robinson, J. A., Dubey, M., Terrones, H. & Terrones, M. Beyond Graphene: Progress in Novel Two-Dimensional Materials and van der Waals Solids. *Annu. Rev. Mater. Res.* **45,** 1–27 (2015).

17. Deng, D. *et al.* Catalysis with two-dimensional materials and their heterostructures. *Nat. Nanotechnol.* **11,** 218–230 (2016).

18. Wang, Y., Li, Y. & Chen, Z. Not your familiar two dimensional transition metal disulfide: structural and electronic properties of the PdS_2 monolayer. *J. Mater. Chem. C* **3,** 9603–9608 (2015).

19. Seh, Z. W. *et al.* Two-Dimensional Molybdenum Carbide (MXene) as an Efficient Electrocatalyst for Hydrogen Evolution. *ACS Energy Lett.* **1,** 589–594 (2016).

20. Wang, Z. *et al.* Chemical Vapor Deposition of Monolayer Mo1−xWxS2 Crystals with Tunable Band Gaps. *Sci. Rep.* **6,** 21536 (2016).

21. Wang, X.-R., Shi, Y. & Zhang, R. Field-effect transistors based on two-dimensional materials for logic applications. *Chinese Phys. B* **22,** 98505 (2013).

22. Mak, K. F., Lee, C., Hone, J., Shan, J. & Heinz, T. F. Atomically thin MoS2: A new direct-gap semiconductor. *Phys. Rev. Lett.* **105,** 2–5 (2010).

23. Voiry, D., Yang, J. & Chhowalla, M. Recent Strategies for Improving the Catalytic Activity of 2D TMD Nanosheets Toward the Hydrogen Evolution Reaction. *Adv. Mater.* 6197–6206 (2016).

24. Xiao, W. *et al.* Dual-Functional N Dopants in Edges and Basal Plane of MoS2 Nanosheets Toward Efficient and Durable Hydrogen Evolution. *Adv. Energy Mater.* **7,** 1–10 (2017).

25. Deng, J. *et al.* Arousing the electrocatalytic hydrogen evolution activity of inert two-dimensional MoS2 surface via single-atom metal doping. *Energy Environ. Sci.* 20–22 (2015).

26. Ma, L. *et al.* Hydrothermal synthesis of selenium-doped graphene-like molybdenum disulfide/graphene hybrid as an efficient electrocatalyst for hydrogen evolution. *Adv. Powder Technol.* **27,** 2153–2160 (2016).

27. Fan, X.-L., Yang, Y., Xiao, P. & Lau, W.-M. Site-specific catalytic activity in exfoliated MoS_2 single-layer polytypes for hydrogen evolution: basal plane and edges. *J. Mater. Chem. A* **2,** 20545–20551 (2014).

28. Šarić, M., Georg, M. P. & Rossmeisl, J. Relation between Hydrogen Evolution and Hydrodesulfurization Catalysis. *ChemCatChem* **8,** 3334–3337 (2016).

29. Cheng, C. C. *et al.* Activating basal-plane catalytic activity of two-dimensional MoS2 monolayer with remote hydrogen plasma. *Nano Energy* **30,** 846–852 (2016).

30. Pan, H. Metal Dichalcogenides Monolayers: Novel Catalysts for Electrochemical Hydrogen Production. *Sci. Rep.* **4,** 1–6 (2014).

31. Cao, L. Layer-Dependent Electrocatalysis of MoS 2 for Hydrogen Evolution. *Nano Lett.* 1–6 (2014).

32. Lu, A. Y. *et al.* High-Sulfur-Vacancy Amorphous Molybdenum Sulfide as a High Current Electrocatalyst in Hydrogen Evolution. *Small* **12,** 5530–5537 (2016).

33. Chua, X. J. *et al.* Negative Electrocatalytic Effects of p-Doping Niobium and Tantalum on MoS2 and WS2 for the Hydrogen Evolution Reaction and Oxygen Reduction Reaction. *ACS Catal.* **6,** 5724–5734 (2016).

34. Putungan, D. B., Lin, S.-H. & Kuo, J.-L. A first-principles examination of conducting monolayer 1T′-MX_2 (M = Mo, W; X = S, Se, Te): promising catalysts for hydrogen evolution reaction and its enhancement by strain. *Phys. Chem. Chem. Phys.* **17,** 21702–21708 (2015).

35. Ambrosi, A., Sofer, Z. & Pumera, M. 2H → 1T phase transition and hydrogen evolution activity of MoS_2 , $MoSe_2$, WS_2 and WSe_2 strongly depends on the MX_2 composition. *Chem. Commun.* **51,** 8450–8453 (2015).

36. Guo, Y., Shang, C., Zhang, X. & Wang, E. Electrocatalytic hydrogen evolution using the MS_2 @MoS_2 /rGO (M = Fe or Ni) hybrid catalyst. *Chem. Commun.* **52,** 11795–11798 (2016).

37. Ouyang, Y. *et al.* Activating Inert Basal Planes of MoS2 for Hydrogen Evolution Reaction through the Formation of Different Intrinsic Defects. *Chem. Mater.* **28,** 4390–4396 (2016).

38. Park, S.-K., Chung, D. Y., Ko, D., Sung, Y.-E. & Piao, Y. Three-dimensional carbon foam/N-doped graphene@MoS_2 hybrid nanostructures as effective electrocatalysts for the hydrogen evolution reaction. *J. Mater. Chem. A* **4,** 12720–12725 (2016).

39. Cummins, D. R. *et al.* Efficient hydrogen evolution in transition metal dichalcogenides via a simple one-step hydrazine reaction. *Nat. Commun.* **7,** 11857 (2016).

40. Chou, S. S. *et al.* Understanding catalysis in a multiphasic two-dimensional transition metal dichalcogenide. *Nat. Commun.* **6,** 8311 (2015).

41. Kong, D. *et al.* Synthesis of MoS_2 and $MoSe_2$ Films with Vertically Aligned Layers. *Nano Lett.* **13,** 1341–1347 (2013).

42. Gao, J. *et al.* Vertically oriented arrays of ReS2 nanosheets for electrochemical energy storage and electrocatalysis. *Nano Lett.* **16,** 3780–3787 (2016).

43. Ye, R. *et al.* High-Performance Hydrogen Evolution from $MoS_{2(1-x)}P_x$ Solid Solution. *Adv. Mater.* **28,** 1427–1432 (2016).

44. Hinnemann, B. *et al.* Biomimetic Hydrogen Evolution: MoS 2 Nanoparticles as Catalyst for Hydrogen Evolution. *J. Am. Chem. Soc.* **127,** 5308–5309 (2005).

45. Lin, L. *et al.* Sulfur-Depleted Monolayered Molybdenum Disulfide Nanocrystals for Superelectrochemical Hydrogen Evolution Reaction. *ACS Nano* **10,** 8929–8937 (2016).

46. Greeley, J., Jaramillo, T. F., Bonde, J., Chorkendorff, I. & Nørskov, J. K. Computational high-throughput screening of electrocatalytic materials for hydrogen evolution. *Nat. Mater.* **5,** 909–913 (2006).

47. Escalera-López, D. *et al.* Enhancement of the Hydrogen Evolution Reaction from Ni-MoS2 Hybrid Nanoclusters. *ACS Catal.* **6,** 6008–6017 (2016).

48. Huang, Z. F. *et al.* Hollow Cobalt-Based Bimetallic Sulfide Polyhedra for Efficient All-pH-Value Electrochemical and Photocatalytic Hydrogen Evolution. *J. Am. Chem. Soc.* **138,** 1359–1365 (2016).

49. Tsai, C., Chan, K., Nørskov, J. K. & Abild-Pedersen, F. Rational design of MoS_2 catalysts: tuning the structure and activity via transition metal doping. *Catal. Sci. Technol.* **5,** 246–253 (2015).

50. Chhowalla, M. *et al.* The chemistry of two-dimensional layered transition metal dichalcogenide nanosheets. *Nat. Chem.* **5,** 263–275 (2013).

51. Choi, Y. H. *et al.* An in Situ Sulfidation Approach for the Integration of MoS2 Nanosheets on Carbon Fiber Paper and the Modulation of Its Electrocatalytic Activity by Interfacing with nC60. *ACS Catal.* **6,** 6246–6254 (2016).

52. Xie, L. M. Two-dimensional transition metal dichalcogenide alloys: preparation, characterization and applications. *Nanoscale* **7,** 18392–18401 (2015).

53. Mohamad Latiff, N. *et al.* Valence and oxide impurities in MoS_2 and WS_2 dramatically change their electrocatalytic activity towards proton reduction. *Nanoscale* **8,** 16752–16760 (2016).

54. Rasmussen, F. A. & Thygesen, K. S. Computational 2D Materials Database: Electronic Structure of Transition-Metal Dichalcogenides and Oxides. *J. Phys. Chem. C* **119,** 13169–13183 (2015).

55. Voiry, D. *et al.* Conducting MoS_2 nanosheets as catalysts for hydrogen evolution reaction. *Nano Lett.* **13,** 6222–7 (2013).

56. Bligaard, T. *et al.* The Brønsted-Evans-Polanyi relation and the volcano curve in heterogeneous catalysis. *J. Catal.* **224,** 206–217 (2004).

57. Jaramillo, T. F. *et al.* Identification of Active Edge Sites for Electrochemical H2 Evolution from MoS2 Nanocatalysts. *Science (80-.).* **317,** 100–102 (2007).

58. Lukowski, M. A. *et al.* Enhanced hydrogen evolution catalysis from chemically exfoliated metallic MoS2 nanosheets. *J. Am. Chem. Soc.* **135,** 10274–10277 (2013).

59. Pandey, M. *et al.* Defect-Tolerant Monolayer Transition Metal Dichalcogenides. *Nano Lett.* **16,** 2234–2239 (2016).

60. Gao, G., Sun, Q. & Du, A. Activating catalytic inert basal plane of molybdenum disulfide to optimize hydrogen evolution activity via defect doping and strain engineering. *J. Phys. Chem. C* **120,** 16761–16766 (2016).

61. Voiry, D. *et al.* The role of electronic coupling between substrate and 2D MoS2 nanosheets in electrocatalytic production of hydrogen. *Nat. Mater.* **15,** 1003–1009 (2016).

62. Hohenberg, P. & Kohn, W. The Inhomogeneous Electron Gas. *Phys. Rev.* **136,** B864 (1964).

63. Kohn, W. & Sham, L. J. Self-consistent equations including exchange and correlation effects. *Phys. Rev.* **140,** (1965).

64. Perdew, J. P. Density-functional approximation for the correlation energy of the inhomogeneous electron gas. *Phys. Rev. B* **33,** 8822–8824 (1986).

65. Becke, A. D. Density-functional exchange-energy approximation with correct asymptotic behavior. *Phys. Rev. A* **38,** 3098–3100 (1988).

66. Perdew, J. P., Burke, K. & Ernzerhof, M. Generalized Gradient Approximation Made Simple. *Phys. Rev. Lett.* **77,** 3865–3868 (1996).

67. Perdew, J. *et al.* Atoms, molecules, solids, and surfaces: Applications of the generalized gradient approximation for exchange and correlation. *Phys. Rev. B* **46,** 6671–6687 (1992).

68. Li, H. *et al.* Kinetic Study of Hydrogen Evolution Reaction over Strained MoS2 with Sulfur Vacancies Using Scanning Electrochemical Microscopy. *J. Am. Chem. Soc.* **138,** 5123–5129 (2016).

69. de Chialvo, M. R. G. & Chialvo, A. C. Hydrogen evolution reaction: Analysis of the Volmer-Heyrovsky-Tafel mechanism with a generalized adsorption model. *J. Electroanal. Chem.* **372,** 209–223 (1994).

70. Tsai, C., Chan, K., Nørskov, J. K. & Abild-Pedersen, F. Theoretical insights into the hydrogen evolution activity of layered transition metal dichalcogenides. *Surf. Sci.* **640,** 133–140 (2015).

71. Trasatti, S. Work function, electronegativity, and electrochemical behaviour of metals. *Electroanal. Chem. Interfacial Electrochem.* **33,** 351–378 (1971).

72. Ishikawa, Y., Mateo, J. J., Tryk, D. A. & Cabrera, C. R. Direct molecular dynamics and density-functional theoretical study of the electrochemical hydrogen oxidation reaction and underpotential deposition of H on Pt(1 1 1). *J. Electroanal. Chem.* **607,** 37–46 (2007).

73. WIKIPEDIA Transition state theory. Available at: https://en.wikipedia.org/wiki/Transition_state_theory.

74. Arrhenius, S. Über die Reaktionsgeschwindigkeit bei der Inversion von Rohrzucker durch Säuren. *Zeitschrift für Phys. Chemie* **4,** 226–248 (1889).

75. Rice, J. An elementary account of the quantum theory. *Trans. Faraday Soc.* **11,** 1–18 (1915).

76. Herzfeld, K. F. Zur Theorie der Reaktionsgeschwindigkeiten in Gasen. *Ann. Phys.* **364,** 635–667 (1919).

77. Trasatti, S. International Union of Pure and Applied Chemistry Commission on Electrochemistry * the Absolute Electrode Potential : an Explanatory Note. *Pure Appl. Chem.* **58,** 955–966 (1986).

78. Trasatti, S. Surface science and electrochemistry: concepts and problems. *Surf. Sci.* **335,** 1–9 (1995).

79. Tsiplakides, D. & Vayenas, C. G. Electrode Work Function and Absolute Potential Scale in Solid-State Electrochemistry. *J. Electrochem. Soc.* **148,** E189 (2001).

80. Bortz, A. B., Kalos, M. H. & Lebowitz, J. L. A New Algorithm for Monte Carlo Simulation of Ising Spin Systems. *J. Comput. Phys.* **17,** 10–18 (1975).

81. WIKIPEDIA Kinetic Monte Carlo. Available at: https://en.wikipedia.org/wiki/Kinetic_Monte_Carlo.

82. Truhlar, D. G. *et al.* Ensemble□averaged variational transition state theory with optimized multidimensional tunneling for enzyme kinetics and other condensed□phase reactions. *Int. J. Quantum Chem.* **100,** 1136–1152 (2004).

83. Masgrau, L. *et al.* Atomic description of an enzyme reaction dominated by proton tunneling. *Science (80-.).* **312,** 237–241 (2006).

84. Reuter, K. & Scheffler, M. First-principles kinetic Monte Carlo simulations for heterogeneous catalysis: Application to the CO oxidation at Ru O2 (110). *Phys. Rev. B - Condens. Matter Mater. Phys.* **73,** 1–17 (2006).

85. Li, H. *et al.* Activating and optimizing MoS2 basal planes for hydrogen evolution through the formation of strained sulphur vacancies. *Nat. Mater.* **15,** 48–53 (2015).

86. Chang, K. *et al.* MoS2/graphene cocatalyst for efficient photocatalytic H 2 evolution under visible light irradiation. *ACS Nano* **8,** 7078–7087 (2014).

87. Tsai, C., Chan, K., Abild-Pedersen, F. & Nørskov, J. K. Active edge sites in MoSe2 and WSe2 catalysts for the hydrogen evolution reaction: a density functional study. *Phys. Chem. Chem. Phys.* **16,** 13156 (2014).

88. Kresse, G. Efficient iterative schemes for ab initio total-energy calculations using a plane-wave basis set. *Physical Review B* **54,** 11169–11186 (1996).

89. Blöchl, P. E. Projector augmented-wave method. *Phys. Rev. B* **50,** 17953–17979 (1994).

90. Lv, H. Y., Lu, W. J., Shao, D. F., Liu, Y. & Sun, Y. P. Strain-controlled switch between ferromagnetism and

antiferromagnetism in 1T-CrX2 (X=Se, Te) monolayers. *Phys. Rev. B - Condens. Matter Mater. Phys.* **92,** 1–8 (2015).

91. Pan, H. Electronic and magnetic properties of vanadium dichalcogenides monolayers tuned by hydrogenation. *J. Phys. Chem. C* **118,** 13248–13253 (2014).

92. Manchanda, P., Sharma, V., Yu, H., Sellmyer, D. J. & Skomski, R. Magnetism of Ta dichalcogenide monolayers tuned by strain and hydrogenation. *Appl. Phys. Lett.* **107,** (2015).

93. ICSD – Inorganic Crystal Structure Database ICSD – reliable crystal structure data.

94. Fuh, H. R., Yan, B., Wu, S. C., Felser, C. & Chang, C. R. Metal-insulator transition and the anomalous Hall effect in the layered magnetic materials VS2 and VSe2. *New J. Phys.* **18,** 1–8 (2016).

95. Lee, J. *et al.* Single- and few-layer WTe_2 and their suspended nanostructures: Raman signatures and nanomechanical resonances. *Nanoscale* **8,** 7854–7860 (2016).

96. Frumkin, A. N. Surface tension curves of higher fatty acids and the equation of condition of the surface layer. *Z. phys. Chem* **116,** 466–484 (1925).

97. Deml, A. M., Holder, A. M., O'Hayre, R. P., Musgrave, C. B. & Stevanović, V. Intrinsic Material Properties Dictating Oxygen Vacancy Formation Energetics in Metal Oxides. *J. Phys. Chem. Lett.* **6,** 1948–1953 (2015).

98. Brett, C. M. A. & Brett, A. M. O. *Electrochemistry, Principles, Methods, and Applications*. (Oxford science publisher, 2000).

99. Léger, J. M., Pereira, A. S., Haines, J., Jobic, S. & Brec, R. Phase transformations of polymeric CdI2-type IrTe2 under high pressure. *J. Phys. Chem. Solids* **61,** 27–34 (2000).

국문 초록

수소는 현재의 화석 연료를 대체할 수 있는 차세대의 청정 에너지원으로 크게 주목을 받고있다. 하지만, 낮은 가격으로 대기를 오염시키지 않으면서 수소를 만들어 내는 것이 중대한 문제이다. 이 점에서 지구상에 풍부한 자원인 물을 분해하여 수소를 만들어 내는 것은 많은 문제들을 해결할 수 있다. 특히 태양광을 이용한 물 분해라면 이상적일 것이다. 전기나 태양광을 이용한 물분해에서의 산소발생반응, 수소발생반응에 요구되는 큰 오버포텐셜을 낮추기 위해서는 촉매의 활용이 필수적이다. 지난 수십년 동안, 백금이 가장 좋은 물 분해의 수소발생반응 촉매로 알려져 왔으나, 이는 매우 비싸기 때문에 대량으로 활용하기에는 적합하지 않다. 그렇기에, 백금을 대체할 수 있는 촉매 물질을 찾기 위한 수많은 연구들이 있었다. 특히, 전이금속칼코겐화합물(TMD)은 수소발생반응을 위한 새로운 이차원 촉매 물질 군으로 주목을 받아왔다. 고효율의 TMD 시스템을 찾기 위한 광범위한 노력 들에도 불구하고 백금을 대체할만한 강력한 후보는 아직 제안되지 않았다. MoS_2 와 같은 TMD 촉매에서 주로 가장자리가 활성 자리라고 여겨졌으나, 이는 전체 시스템에서 한정된 부분을 차지하는 자리이기 때문에 한계가 있었다. 그러나 최근에는, MoS_2 의 기저 표면도 황 원자의 공공 자리를 만들고 인장

변형을 가해준다면 충분히 활성화될 수 있다는 것이 밝혀진 바 있다. 본 연구에서는, 제일원리계산에서의 에너지 관계를 이용한 키네틱몬테카를로 시뮬레이션을 이용하여 공공 자리에서 발생하는 수소발생반응의 메커니즘을 밝히고자 하였다. 이로써, MoS_2 의 황 공공 자리에서의 수소발생반응은 Volmer-Heyrovsky 메커니즘을 따르고, 공공 자리가 전자를 축적함으로써 반응속도를 결정하는 스텝인 Heyrovsky 스텝의 에너지 장벽을 낮출 수 있다는 것을 밝혔다. 게다가, 인장 변형이 가해졌을 때, 더욱 전자를 축적하기가 쉬워져 추가적으로 에너지 장벽을 낮출 수 있다는 것을 보였다. 또한 본 연구에서는, 제일원리계산을 통한 스크리닝 연구를 통하여 수소발생반응을 위한 새로운 TMD 촉매를 제안하고자 하였다. 우리는 다양한 TMD 물질들의 완벽한 기저 표면과 결함이 존재하는 기저 표면에 대해서 수소흡착에너지를 디스크립터로 활용하여 수소발생반응 촉매 효율을 조사하였다. 수소흡착에너지가 공공의 농도에 따라 변한다는 것을 알았고, 각각의 농도 조건에서 높은 촉매 성능을 보일 것으로 예상되는 좋은 후보 물질을 발견하였다. 낮은 농도 조건에서는 $ZrSe_2$ 와 $ZrTe_2$ 를, 중간 혹은 높은 농도의 공공 조건이 가능하다면 $MoSe_2$, $MoTe_2$, WSe_2, $ReTe_2$, MoS_2 그리고 $ReSe_2$ 룰 좋은 촉매로 제안한다. 이 물질들로써 우리는 변형을 가하지 않고도 백금에 대적할만한 높은 효율을 얻을 수 있을 것이라

기대한다. 추가적으로 다중선형회귀분석을 통하여 TMD 에서 음이온 공공의 형성 에너지 그 결함을 갖는 시스템의 전자 구조가 수소발생반응 효율의 디스크립터로 평가되는 수소흡착에너지와 큰 상관관계를 갖는다는 것을 밝혔다.

주요어: 제일원리계산, 키네틱몬테카를로, 수소발생반응, 전이금속칼코겐화합물, 결함, 메커니즘, 반응속도론, 스크리닝

학 번 : 2013-30184